THE *HUBBLE SPACE TELESCOPE*[*] CLUSTER SUPERNOVA SURVEY: THE TYPE Ia SUPERNOVA RATE IN HIGH-REDSHIFT GALAXY CLUSTERS

K. BARBARY[1,2], G. ALDERING[2], R. AMANULLAH[1,3], M. BRODWIN[4,5], N. CONNOLLY[6], K. S. DAWSON[2,7], M. DOI[8], P. EISENHARDT[9], L. FACCIOLI[2], V. FADEYEV[10], H. K. FAKHOURI[1,2], A. S. FRUCHTER[11], D. G. GILBANK[12], M. D. GLADDERS[13], G. GOLDHABER[1,2,26], A. GOOBAR[3,14], T. HATTORI[15], E. HSIAO[2], X. HUANG[1], Y. IHARA[8,25], N. KASHIKAWA[16], B. KOESTER[13,17], K. KONISHI[18], M. KOWALSKI[19], C. LIDMAN[20], L. LUBIN[21], J. MEYERS[1,2], T. MOROKUMA[8,16,25], T. ODA[22], N. PANAGIA[11], S. PERLMUTTER[1,2], M. POSTMAN[11], P. RIPOCHE[2], P. ROSATI[23], D. RUBIN[1,2], D. J. SCHLEGEL[2], A. L. SPADAFORA[2], S. A. STANFORD[21,24], M. STROVINK[1,2], N. SUZUKI[2], N. TAKANASHI[16], K. TOKITA[8], N. YASUDA[18]
(THE SUPERNOVA COSMOLOGY PROJECT)
Submitted to the Astrophysical Journal

ABSTRACT

We report a measurement of the Type Ia supernova (SN Ia) rate in galaxy clusters at $0.9 < z < 1.45$ from the *Hubble Space Telescope (HST)* Cluster Supernova Survey. This is the first cluster SN Ia rate measurement with detected $z > 0.9$ SNe. Finding 8 ± 1 cluster SNe Ia, we determine a SN Ia rate of $0.50^{+0.23}_{-0.19}$ (stat) $^{+0.10}_{-0.09}$ (sys) h_{70}^2 SNuB (SNuB $\equiv 10^{-12}$ SNe $L_{\odot,B}^{-1}$ yr^{-1}). In units of stellar mass, this translates to $0.36^{+0.16}_{-0.13}$ (stat) $^{+0.07}_{-0.06}$ (sys) h_{70}^2 SNuM (SNuM $\equiv 10^{-12}$ SNe $M_{\odot}^{-1}$ yr^{-1}). This represents a factor of $\approx 5 \pm 2$ increase over measurements of the cluster rate at $z < 0.2$. We parameterize the late-time SN Ia delay time distribution with a power law: $\Psi(t) \propto t^s$. Under the assumption of a cluster formation redshift of $z_f = 3$, our rate measurement in combination with lower-redshift cluster SN Ia rates constrains $s = -1.31^{+0.55}_{-0.40}$, consistent with measurements of the delay time distribution in the field. This measurement is also consistent with the value of $s \approx -1$ typically expected for the "double degenerate" SN Ia progenitor scenario, and inconsistent with some models for the "single degenerate" scenario predicting a steeper delay time distribution at large delay times. We check for environmental dependence and the influence of younger stellar populations by calculating the rate specifically in cluster red-sequence galaxies and in morphologically early-type galaxies, finding results similar to the full cluster rate. Finally, the upper limit of one host-less cluster SN Ia detected in the survey implies that the fraction of stars in the intra-cluster medium is less than 0.47 (95% confidence), consistent with measurements at lower redshifts.

Subject headings: Supernovae: general — white dwarfs — cosmology: observations

kbarbary@berkeley.edu

[*] Based in part on observations made with the NASA/ESA *Hubble Space Telescope*, obtained from the data archive at the Space Telescope Institute. STScI is operated by the association of Universities for Research in Astronomy, Inc. under the NASA contract NAS 5-26555. The observations are associated with program GO-10496.

[1] Department of Physics, University of California, Berkeley, CA 94720

[2] E. O. Lawrence Berkeley National Lab, 1 Cyclotron Rd., Berkeley, CA 94720

[3] The Oskar Klein Centre for Cosmo Particle Physics, AlbaNova, SE-106 91 Stockholm, Sweden

[4] Harvard-Smithsonian Center for Astrophysics, 60 Garden Street, Cambridge, MA 02138

[5] W. M. Keck Postdoctoral Fellow at the Harvard-Smithsonian Center for Astrophysics

[6] Hamilton College Department of Physics, Clinton, NY 13323

[7] Department of Physics and Astronomy, University of Utah, Salt Lake City, UT 84112

[8] Institute of Astronomy, Graduate School of Science, University of Tokyo 2-21-1 Osawa, Mitaka, Tokyo 181-0015, Japan

[9] Jet Propulsion Laboratory, California Institute of Technology, Pasadena, CA 91109

[10] Santa Cruz Institute for Particle Physics, University of California, Santa Cruz, CA 94064

[11] Space Telescope Science Institute, 3700 San Martin Drive, Baltimore, MD 21218

[12] Department of Physics and Astronomy, University Of Waterloo, Waterloo, Ontario, Canada N2L 3G1

[13] Department of Astronomy and Astrophysics, University of Chicago, Chicago, IL 60637

[14] Department of Physics, Stockholm University, Albanova University Center, SE-106 91, Stockholm, Sweden

[15] Subaru Telescope, National Astronomical Observatory of Japan, 650 North A'ohaku Place, Hilo, HI 96720

[16] National Astronomical Observatory of Japan, 2-21-1 Osawa, Mitaka, Tokyo,181-8588, Japan

[17] Kavli Institute for Cosmological Physics, The University of Chicago, Chicago IL 60637

[18] Institute for Cosmic Ray Research, University of Tokyo, 5-1-5, Kashiwanoha, Kashiwa, Chiba, 277-8582, Japan

[19] Physikalisches Institut, Universität Bonn, Bonn, Germany

[20] Australian Astronomical Observatory, PO Box 296, Epping, NSW 1710, Australia

[21] University of California, Davis, CA 95618

[22] Department of Astronomy, Kyoto University, Sakyo-ku, Kyoto 606-8502, Japan

[23] ESO, Karl-Schwarzschild-Strasse 2, D-85748 Garching, Germany

[24] Institute of Geophysics and Planetary Physics, Lawrence Livermore National Laboratory, Livermore, CA 94550

[25] JSPS Fellow

[26] Deceased

1. INTRODUCTION

Type Ia supernovae (SNe Ia) are widely accepted to be the result of the thermonuclear explosion of a carbon-oxygen (CO) white dwarf (WD). The explosion is believed to occur as the WD nears the Chandrasekhar mass by accreting mass from its companion star in a binary system. Despite the confidence in this basic model, many uncertainties remain about the process that leads to SNe Ia (see Livio 2001, for a review). Chief amongst them is the nature of the companion donor star. The leading models fall into two classes: the *single degenerate* scenario (SD; Whelan & Iben 1973), and the *double degenerate* scenario (DD; Iben & Tutukov 1984; Webbink 1984). In the SD scenario the companion is a red giant or main sequence star that overflows its Roche lobe. In the DD scenario, the companion is a second WD which merges with the primary after orbital decay due to the emission of gravitational radiation.

A better understanding of the SN Ia progenitor is demanded from both an astrophysical and a cosmological perspective. Astrophysically, SNe Ia dominate the production of iron (e.g., Matteucci & Greggio 1986; Tsujimoto et al. 1995; Thielemann et al. 1996) and provide energy feedback (Scannapieco et al. 2006) in galaxies. Knowledge of the SN Ia rate is necessary to include these effects in galaxy evolution models. However, an accurate prediction of the SN Ia rate in galaxies of varying ages, masses and star formation histories requires a good understanding of the progenitor process. This is particularly true for higher redshifts where direct SN rate constraints are unavailable. From a cosmological perspective, the progenitor has become a central concern following the use of SNe Ia as standardizable candles in the discovery of dark energy (Riess et al. 1998; Perlmutter et al. 1999). With hundreds of SNe now being used in the precision measurement of cosmological parameters (e.g., Hicken et al. 2009; Amanullah et al. 2010), astrophysical sources of systematic error will soon become significant. While the unknown nature of the SN progenitor system is unlikely to bias measurements at the current level of uncertainty (Yungelson & Livio 2000; Sarkar et al. 2008), it could become a significant source of uncertainty in the future, as it leaves open the question of whether high-redshift SNe are different than low-redshift SNe in a way that affects the inferred distance.

Measuring the SN Ia rate as a function of environment has long been recognized as one of the few available methods for probing the SN Ia progenitor (e.g., Ruiz-Lapuente et al. 1995; Ruiz-Lapuente & Canal 1998; Yungelson & Livio 2000). SN Ia rates constrain the progenitor scenario via the delay time distribution (DTD), where "delay time" refers to the time between star formation and SN Ia explosion. The DTD is the distribution of these times for a population of stars, and is equivalent to the SN Ia rate as a function of time after a burst of star formation. The delay time is governed by different physical mechanisms in the different progenitor scenarios. For example, in the SD scenario, when the donor is a red giant star the delay time is set by the time the companion takes to evolve off the main sequence. In the DD scenario, it is dominated by the time the orbit takes to decay due to gravitational radiation. The result is that the shape of the DTD depends on the progenitor scenario.

However, the interpretation of the DTD is complicated by its dependence on other factors, not all of which are completely understood. These include the initial mass function (IMF) of the stellar population, the distribution of initial separation and mass ratio in binary systems, and the evolution of the binary through one or more common envelope (CE; see, e.g., Yungelson 2005) phases. Theoretical delay time distributions were computed analytically following the proposal of both the SD (Greggio & Renzini 1983) and DD (Tornambe & Matteucci 1986; Tornambe 1989) scenarios. Later, theoretical DTDs were extended to include various subclasses of each model and a wider range of parameters (Tutukov & Yungelson 1994; Yungelson & Livio 2000; Matteucci & Recchi 2001; Belczynski et al. 2005; Greggio 2005). In various recent numerical simulations, different plausible prescriptions for the initial conditions and for the binary evolution have lead to widely ranging DTDs, even within one scenario (Hachisu et al. 2008; Kobayashi & Nomoto 2009; Ruiter et al. 2009; Mennekens et al. 2010). A measurement of the DTD then must constrain not only the relative contribution of various progenitor scenarios, but also the initial conditions and CE phase, which is particularly poorly constrained. Still, most simulations show a difference in the DTD shape between the SD and DD scenarios. In both scenarios, the SN rate is greatest shortly after star formation and gradually decreases with time. However, the SD scenario typically shows a strong drop off in the SN rate at large delay times not seen in the DD scenario (but see Hachisu et al. 2008).

The DTD can be measured empirically from the SN Ia rate in stellar populations of different ages. Measurements correlating SN rate with host star formation rate or star formation history have now confirmed that the delay time spans a wide range, from less than 100 Myr (e.g., Aubourg et al. 2008) to many Gyr (e.g., Schawinski 2009). Correlations with star formation rates (Mannucci et al. 2005, 2006; Sullivan et al. 2006; Pritchet et al. 2008) show that SNe with progenitor ages $\lesssim$ a few hundred Myr comprise perhaps $\sim$50% of all SNe Ia. Measurements as a function of stellar age (Totani et al. 2008; Brandt et al. 2010), show that the rate declines with delay time as expected.

It is more straightforward to extract the DTD in stellar populations with a narrow range of ages (with a single burst of star formation being the ideal). Galaxy clusters, which are dominated by early-type galaxies, provide an ideal environment for constraining the shape of the DTD at large delay times. Early-type galaxies are generally expected to have formed early ($z \gtrsim 2$) with little star formation since (Stanford et al. 1998; van Dokkum et al. 2001). Cluster early-type galaxies in particular form even earlier than those in the field, with most star formation occurring at $z \gtrsim 3$ (Thomas et al. 2005; Sánchez-Blázquez et al. 2006; Gobat et al. 2008). Measuring the cluster SN Ia rate over a range of redshifts from $z = 0$ to $z > 1$ provides a measurement of the SN Ia rate at delay times from $\sim$2 to 11 Gyr. Obtaining an accurate rate at the highest-possible redshift is crucial for constraining the shape of the late-time DTD: a larger redshift range corresponds to a larger lever arm in delay time.

In addition to DTD constraints, there are also strong motivations for measuring the cluster SN Ia rate from a perspective of cluster studies. SNe Ia are an important source of iron in the intracluster medium (e.g., Loewenstein 2006). Cluster SN rates constrain the iron contribution from SNe and, paired with measured iron abundances, can also constrain possible enrichment mechanisms (Maoz & Gal-Yam 2004). The high-redshift cluster rate is particularly important: measurements show that most of the intracluster iron was produced at high redshift (Calura et al. 2007). The poorly-constrained high-

redshift cluster rate is one of the largest sources of uncertainty in constraining the metal-loss fraction from galaxies (Sivanandam et al. 2009).

Cluster SNe Ia can also be used to trace the diffuse *intracluster* stellar component. Intracluster stars, bound to the cluster potential rather than individual galaxies, have been found to account for anywhere from 5% to 50% of the stellar mass in clusters (e.g., Ferguson et al. 1998; Feldmeier et al. 1998; Gonzalez et al. 2000; Feldmeier et al. 2004; Lin & Mohr 2004; Zibetti et al. 2005; Gonzalez et al. 2005; Krick et al. 2006; Mihos et al. 2005). The use of SNe Ia as tracers of this component was first demonstrated by Gal-Yam et al. (2003) who found two likely host-less SNe Ia out of a total of seven cluster SNe Ia in $0.06 < z < 0.19$ Abell clusters. After correcting for the greater detection efficiency of host-less SNe, they determined that on average, the intracluster medium contained 20^{+20}_{-12}% of the total cluster stellar mass. The intrinsic faintness of the light from intracluster stars, combined with $(1+z)^4$ surface brightness dimming, makes surface brightness measurements impossible at redshifts much higher than $z = 0.3$. Type Ia supernovae, which are detectable up to and beyond $z = 1$, provide a way to measure the intracluster stellar component and its possible evolution with redshift.

The cluster SN Ia rate has recently been measured at lower redshifts ($z > 0.3$) in several studies (Sharon et al. 2007; Mannucci et al. 2008; Dilday et al. 2010), and at intermediate redshift ($z \sim 0.6$) by Sharon et al. (2010). However, at higher redshifts ($z \gtrsim 0.8$), only weak constraints on the high-redshift cluster Ia rate exist, based on 1–2 SNe Ia at $z = 0.83$ (Gal-Yam et al. 2002). In this paper, we calculate the SN Ia rate in $0.9 < z < 1.45$ clusters observed in the *HST* Cluster Supernova Survey. We address the host-less SN Ia fraction, and use our result to place constraints on the late-time DTD in clusters. Maoz et al. (2010, hereafter Maoz10) have already combined our results with iron abundance measurements and rate measurements in other environments to place even tighter constraints on the SN Ia DTD.

This paper is organized as follows. In §2 we review the survey, placing particular emphasis on the aspects relevant to the rate calculation. In §3 we describe the selection of supernova candidates used in this rate calculation and the determination of supernova type for these candidates. In §4 we carry out efficiency studies to determine the detection efficiency of our SN selection. In §5 we measure the luminosity of the clusters based on data from the survey. In §6 we present results and characterize systematic errors. We discuss interpretations for the delay time distribution and conclude in §7. Throughout the paper we use a cosmology with $H = 70$ km s^{-1} Mpc^{-1}, $\Omega_M = 0.3$, $\Omega_\Lambda = 0.7$. Unless otherwise noted, magnitudes are in the Vega system.

This is one of a series of papers presenting supernova results from the *HST* Cluster Supernova Survey (PI Perlmutter; *HST* program GO-10496). The survey design, supernova search, spectroscopic confirmation, and an initial list of supernova candidates is described in Dawson et al. (2009, hereafter Dawson09). Additional spectroscopy is reported in Morokuma et al. (2010), and ground-based IR photometry is reported in Melbourne et al. (2007). Several other papers are either submitted or in preparation, including a detailed study of the cluster and SN host environments (Meyers et al., hereafter Meyers10), a determination of the NICMOS zeropoint for faint sources (Ripoche et al.), and light curve fitting and

cosmological constraints (Suzuki et al.) The volumetric (non-cluster) SN rate from the survey will also be presented in a separate paper (Barbary et al.) using the SN selection and typing presented here.

2. THE SURVEY

The details of the *HST* Cluster SN Survey are described in Dawson09. Here, we briefly summarize the survey and highlight the details relevant to the rate calculation. The survey targeted 25 massive galaxy clusters in a rolling search between July 2005 and December 2006. Clusters were selected from X-ray, optical and IR surveys and cover the redshift range $0.9 < z < 1.45$. Twenty-four of the clusters have spectroscopically confirmed redshifts and the remaining cluster has a photometric redshift estimate. Cluster positions, redshifts and discovery methods are listed in Table 1. Note that cluster positions differ slightly from those reported in Dawson09 due to the use of an updated algorithm for determining cluster centers.

During the survey, each cluster was observed once every 20 to 26 days during its *HST* visibility window (typically four to seven months). Figure 1 shows the dates of visits to each cluster. Each visit consisted of four exposures in the F850LP filter (hereafter z_{850}). Most visits also included a fifth exposure in the F775W filter (hereafter i_{775}). We revisited clusters D, N, P, Q, R and Z towards the end of the survey when they became visible again.

Immediately following each visit, the four z_{850} exposures were cosmic ray-rejected and combined using MULTIDRIZZLE (Fruchter & Hook 2002; Koekemoer et al. 2002) and searched for supernovae. Following the technique employed in the earliest Supernova Cosmology Project searches (Perlmutter et al. 1995, 1997), we used the initial visit as a reference image, flagged candidates with software and then considered them by eye. Likely supernovae were followed up spectroscopically using pre-scheduled time on the Keck, VLT and Subaru telescopes. For nearly all SN candidates, either a live SN spectrum or host galaxy spectrum was obtained. In many cases, spectroscopy of cluster galaxies was obtained contemporaneously using slit masks. Candidates deemed likely to be at higher redshift ($z > 1$) were also observed with the NICMOS camera on *HST*, but these data are not used in this work.

A number of visits were contingent on the existence of an active SN. At the end of a cluster's visibility window, the last two scheduled visits were cancelled if there was no live SN previously discovered. This is because a SN discovered on the rise in either of the last two visits could not be followed long enough to obtain a cosmologically useful light curve. In addition, supplementary visits between pre-scheduled visits were occasionally added to provide more complete light curve information for SNe (in the case of clusters A, C, Q, and U). We call all visits contingent on the existence of an active SN "follow-up" visits (designated by open circles in Fig. 1).

3. SUPERNOVA SELECTION

During the survey, our aim was to find as many supernovae as possible and find them as early as possible in order to trigger spectroscopic and NICMOS followup. Thus, software thresholds for flagging candidates for consideration were set very low, and all possible supernovae were carefully considered by a human screener. Over the course of the survey, thresholds were changed and the roster of people scanning the

Barbary et al.

Table 1
Cluster positions and redshifts

ID	Cluster	Redshift	R.A. (J2000)	Decl. (J2000)	Discovery
A	XMMXCS J2215.9-1738	1.45	$22^h\ 15^m\ 59^s.0$	$-17°\ 37'\ 59''$	X-ray
B	XMMU J2205.8-0159	1.12	$22^h\ 05^m\ 50^s.6$	$-01°\ 59'\ 30''$	X-ray
C	XMMU J1229.4+0151	0.98	$12^h\ 29^m\ 29^s.2$	$+01°\ 51'\ 21''$	X-ray
D	RCS J0221.6-0347	1.02	$02^h\ 21^m\ 42^s.2$	$-03°\ 21'\ 52''$	Optical
E	WARP J1415.1+3612	1.03	$14^h\ 15^m\ 11^s.1$	$+36°\ 12'\ 03''$	X-ray
F	ISCS J1432.4+3332	1.11	$14^h\ 32^m\ 28^s.1$	$+33°\ 33'\ 00''$	IR-Spitzer
G	ISCS J1429.3+3437	1.26	$14^h\ 29^m\ 17^s.7$	$+34°\ 37'\ 18''$	IR-Spitzer
H	ISCS J1434.4+3426	1.24	$14^h\ 34^m\ 28^s.6$	$+34°\ 26'\ 22''$	IR-Spitzer
I	ISCS J1432.6+3436	1.34	$14^h\ 32^m\ 38^s.8$	$+34°\ 36'\ 36''$	IR-Spitzer
J	ISCS J1434.7+3519	1.37	$14^h\ 34^m\ 46^s.0$	$+35°\ 19'\ 36''$	IR-Spitzer
K	ISCS J1438.1+3414	1.41	$14^h\ 38^m\ 08^s.2$	$+34°\ 14'\ 13''$	IR-Spitzer
L	ISCS J1433.8+3325	1.37	$14^h\ 33^m\ 51^s.1$	$+33°\ 25'\ 50''$	IR-Spitzer
M	Cl J1604+4304	0.92	$16^h\ 04^m\ 23^s.8$	$+43°\ 04'\ 37''$	Optical
N	RCS J0220.9-0333	1.03	$02^h\ 20^m\ 55^s.5$	$-03°\ 33'\ 10''$	Optical
P	RCS J0337.8-2844	1.1[a]	$03^h\ 37^m\ 51^s.2$	$-28°\ 44'\ 58''$	Optical
Q	RCS J0439.6-2904	0.95	$04^h\ 39^m\ 37^s.6$	$-29°\ 05'\ 01''$	Optical
R	XLSS J0223.0-0436	1.22	$02^h\ 23^m\ 03^s.4$	$-04°\ 36'\ 14''$	X-ray
S	RCS J2156.7-0448	1.07	$21^h\ 56^m\ 42^s.2$	$-04°\ 48'\ 04''$	Optical
T	RCS J1511.0+0903	0.97	$15^h\ 11^m\ 03^s.5$	$+09°\ 03'\ 09''$	Optical
U	RCS J2345.4-3632	1.04	$23^h\ 45^m\ 27^s.2$	$-36°\ 32'\ 49''$	Optical
V	RCS J2319.8+0038	0.91	$23^h\ 19^m\ 53^s.4$	$+00°\ 38'\ 13''$	Optical
W	RX J0848.9+4452	1.26	$08^h\ 48^m\ 56^s.4$	$+44°\ 52'\ 00''$	X-ray
X	RDCS J0910+5422	1.11	$09^h\ 10^m\ 45^s.1$	$+54°\ 22'\ 07''$	X-ray
Y	RDCS J1252.9-2927	1.23	$12^h\ 52^m\ 54^s.4$	$-29°\ 27'\ 17''$	X-ray
Z	XMMU J2235.3-2557	1.39	$22^h\ 35^m\ 20^s.8$	$-25°\ 57'\ 39''$	X-ray

References. — A (Stanford et al. 2006; Hilton et al. 2007); B,C (Bohringer et al. 2005; Santos et al. 2009); D (also known as RzCS 052; Andreon et al. 2008a,b); D, N, U (Gilbank et al. in prep); E (Perlman et al. 2002); F (Elston et al. 2006); G, I, J, L (Eisenhardt et al. 2008); L (Brodwin et al. in prep; Stanford et al. in prep); H (Brodwin et al. 2006); K (Stanford et al. 2005); M (Postman et al. 2001); Q (Cain et al. 2008); R (Andreon et al. 2005; Bremer et al. 2006); S (Hicks et al. 2008); V (Gilbank et al. 2008); W (Rosati et al. 1999); X (Stanford et al. 2002); Y (Rosati et al. 2004); Z (Mullis et al. 2005; Rosati et al. 2009).

Note. — Cluster positions differ slightly from those reported in Dawson09 due to the use of an updated algorithm for determining cluster centers.

[a] photometric redshift

subtractions changed. As a result, the initial candidate selection process was inclusive but heterogeneous, and depended heavily on human selection. This made it difficult to calculate a selection efficiency for the SN candidates selected during the survey (listed in Tables 3 and 4 of Dawson09).

In this section, we select an independent SN candidate sample (without regard for the Dawson09 sample) using automated selection wherever possible. Although the remainder of this paper will focus on cluster SNe, candidates are selected without regard for cluster membership (which is only known from follow-up spectroscopy once the candidate has already been found) and we determine SN types for both cluster and non-cluster SNe. The non-cluster SNe are considered further in a second paper deriving the volumetric SN Ia field rate (Barbary et al., in preparation). The automated selection consists of initial detection in pairs of subtracted images (§3.1; 86 candidates selected), and subsequent requirements based on the light curve of each candidate (§3.2; 60 candidates remaining). The selection efficiency for these two steps is later calculated via a Monte Carlo simulation. In §3.3 we assign a type (SN Ia, core-collapse SN, or other) to each of the remaining 60 candidates based on all data available (including triggered follow-up observations). For this last step we do not calculate an efficiency or completeness. Instead we estimate the classification uncertainty of the assigned type for each candidate individually. For most candidates the uncertainty in the type is negligible thanks to ample photometric and spectroscopic data.

3.1. *Initial detection*

For the purpose of initially detecting candidates, we use only "search" visits (filled circles in Fig. 1) and disregard the "follow-up" visits (open circles in Fig. 1). (In the following section we will use any available "follow-up" visits to construct more complete light curves for the candidates discovered in this section.) We use the MULTIDRIZZLE-combined, cosmic ray-rejected, z_{850} image from each "search" visit. We consider only regions in this image that are covered by three or more z_{850} exposures. With less than three exposures, the combined images are too heavily contaminated by cosmic rays to be practically searchable for SNe. Although there are typically four z_{850} exposures, the dither pattern used in the survey means that not all regions of the combined image have four exposures. The ACS camera is a mosaic of two 2048×4096 pixel CCD chips (1 pixel = $0.05''$) separated by $2.5''$. The z_{850} exposures were dithered to cover this gap, meaning that a $5''$ wide region in the center of the image and $2.5''$ wide regions on either side of the image are only covered by two exposures and thus are not searchable. Due to orbital constraints, the position angle of *HST* changes between each visit. This means that the unsearchable "gap" region rotates over the field between visits, and that the outer parts of the field are observed in some visits, but not others (Fig. 2, second row). The regions around bright stars are also considered "not searchable" and are similarly masked.

For each "search" visit to each cluster, we follow these four steps:

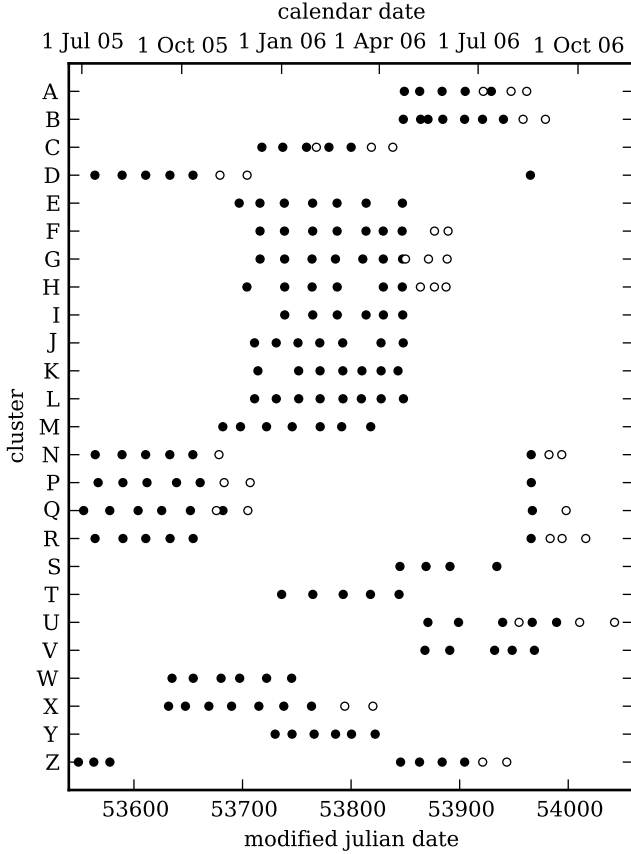**1. A reference image is made** by combining images from

Figure 1. Dates of visits to each cluster. All visits included z_{850} exposures (usually four). Most visits also included one i_{775} exposure. Filled circles indicate "search" visits (used for finding SNe). Open circles indicate "followup" visits (contingent on the existence of an active SN candidate). Clusters D, N, P, Q and R were re-visited once towards the end of the survey, with additional follow-up visits devoted to clusters in which promising SN candidates were found (N, Q, R).

Table 2
Light Curve Requirements

Requirement	Candidates Remaining
Before light curve requirements	86
Positive i_{775} flux (if observed in i_{775})	81
2σ Detection in surrounding epochs	73
If declining, Require two 5σ detections	60

greater in a 3 pixel radius aperture in three or more individual exposures.

- Individual exposures: A candidate cannot have an individual exposure with a flux more than 20σ greater than the flux in the lowest flux exposure *and* a second individual exposure with flux more than 10σ greater than the flux in the lowest flux exposure.

The first requirement is designed to eliminate low significance detections on bright galaxies. The second requirement helps eliminate dipoles on bright galaxy cores caused by slight image misalignment. The third and fourth requirements are aimed at false detections due to cosmic ray coincidence. They require the candidate to be detected in most of the exposures and allow no more than one exposure to be greatly affected by a cosmic ray. On the order of five to ten candidates per subtraction pass all the requirements, resulting in approximately 1000 candidates automatically flagged across the 155 search visits.

4. Each candidate is evaluated by eye in the subtraction. Because the position angle changes between each epoch, the orientation of stellar diffraction spikes changes, causing the majority of the false detections. These are easy to detect and eliminate by eye. Occasionally there are mis-subtractions on the cores of bright galaxies that pass the above requirements. Only completely unambiguous false detections are eliminated in this step. If there is any possibility the candidate is a real SN, it is left in the sample for further consideration.

After carrying out the above four steps for all 155 search visit, 86 candidates remain. At this point, candidates have been selected based only on information from a single z_{850} subtraction.

3.2. *Lightcurve Requirements*

The 86 remaining candidates still include a considerable number of non-SNe. We wish to trim the sample down as much as possible in an automated way, so that we can easily calculate the efficiency of our selection. For each candidate, we now make three further automated requirements based on i_{775} data (if available) and the shape of the z_{850} light curve. The requirements and number of candidates remaining after each requirement are summarized in Table 2.

First, we require that if i_{775} data exists for the epoch in which the candidate was detected, there be positive flux in a 2 pixel radius aperture at the candidate location in the i_{775} image. From our SN light curve simulations, we find that virtually all SNe should pass (near maximum light there is typically enough SN flux in the i_{775} filter to result in a positive total flux, even with large negative sky fluctuations). Meanwhile, about half of the cosmic rays located far from galaxies will fail this test (due to negative sky fluctuations). If there is no i_{775} data for the detection epoch, this requirement is not applied. Even though nearly all SNe are expected to pass, we
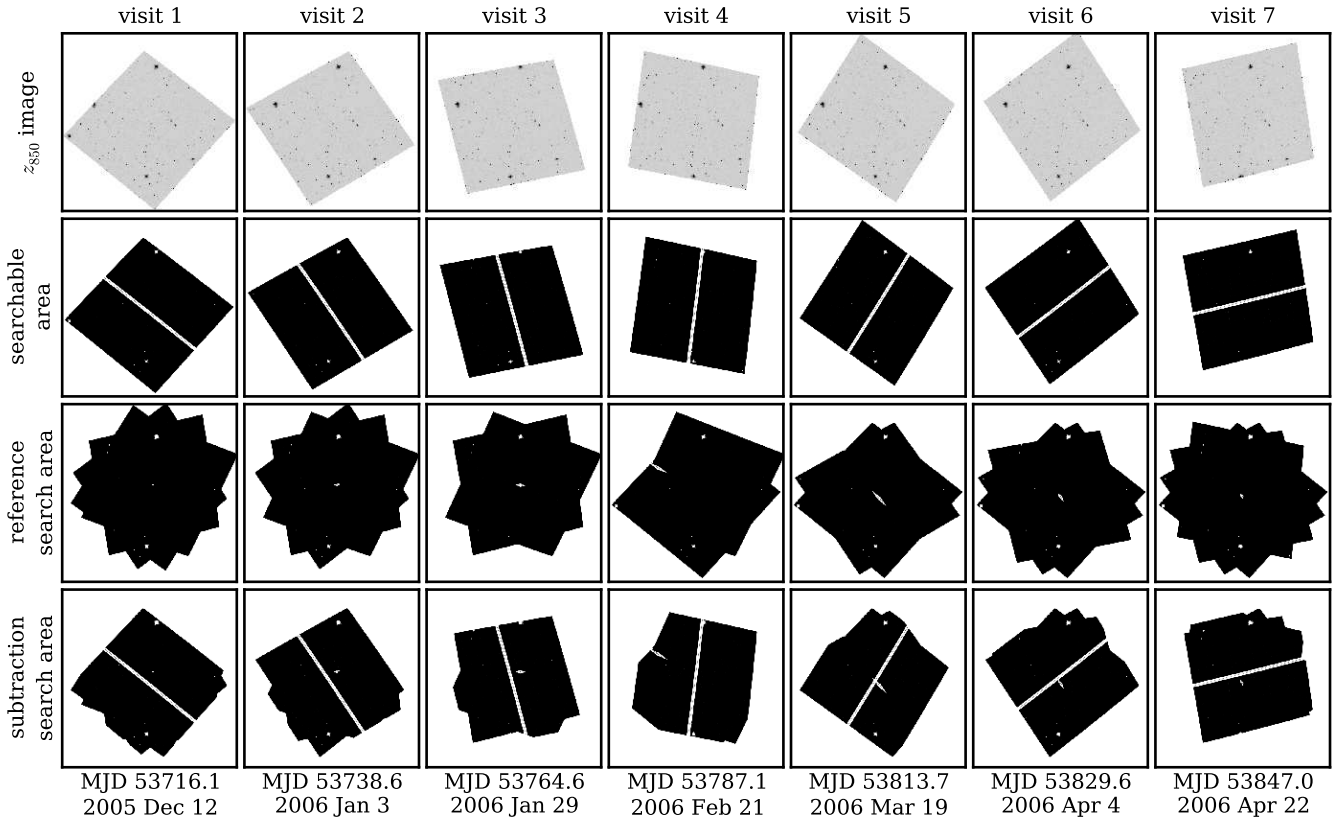
other visits to the cluster. All visits that are either 50 or more days before the search epoch or 80 or more days after the search epoch are included. If there are no epochs outside this 130 day range, the range is narrowed symmetrically until one epoch qualifies. Masked pixels in each visit's image do not contribute to the stacked reference image (Fig. 2, third row).

2. A subtracted image is made by subtracting the stacked reference image from the search epoch image. A map of the sky noise level in the subtraction is made by considering the noise level of the search epoch image and the noise level of each reference image contributing to a given region. Any area masked in either the search epoch or stacked reference image is masked in the subtracted image (Fig. 2, fourth row).

3. Candidates in the subtraction are identified by software. To be flagged, a candidate must have three contiguous pixels with a flux 3.4 times the local sky noise level in the subtraction (as determined by the sky noise map above). Once flagged, it must fulfill the following four requirements:

- MULTIDRIZZLE-combined image: A total signal-to-noise ratio (including sky and Poisson noise) of 5 or more in a 3 pixel radius aperture.

- MULTIDRIZZLE-combined image: A total signal-to-noise ratio of 1.5 or more in a 10 pixel radius aperture.

- Individual exposures: A signal-to-noise ratio of 1 or

Figure 2. An example of image orientation and searchable regions for cluster ISCS J1432.4+3332. Each column represents an observation of the cluster. The first row is the z_{850} image for that visit. The second row is the part of that image that is searchable. The third row shows the searchable area of the stacked reference image used in the subtraction for this visit. The fourth row is the searchable area in the subtraction (the intersection of the second and third rows).

account for any real SNe that would be removed in our Monte Carlo simulation.

Second, we require that the light curve does not rise and fall too quickly: if there is a "search" visit less than 60 days before the detection visit and also one less than 60 days after the detection visit, the candidate must be detected at a 2σ level in at least one of these two visits. SNe Ia have light curves wide enough to be detected at this level in two epochs spaced apart by 60 days. However, cosmic rays in one z_{850} image are unlikely to be repeated in the same spot in two epochs and thus will be removed. This requirement is also included in our Monte Carlo simulation.

The third and final requirement aims to eliminate candidates that were significantly detected in only the first epoch and that then faded from view. Such candidates would not have been followed up spectroscopically and it would typically be impossible to tell if such candidates were SNe (and if so, Type Ia or core collapse) on the basis of a single detection. We chose to eliminate any such candidates and account for this elimination in our Monte Carlo simulation, rather than dealing with an "untypeable" candidate. Specifically, if a candidate is found on the decline (in the first search epoch), we require two epochs with 5σ detections. For high-redshift ($z \sim 1$) SNe Ia, this requirement means that the first epoch will be at approximately maximum light, and most of the SN decline is captured, making it possible to confirm a SN and estimate a type. For candidates that are only significantly detected in the last search epoch, typing is not a problem because additional ACS orbits were typically scheduled in order to follow such candidates.

After these requirements 60 candidates remain. The automatic selection means that we can easily calculate the completeness of the selection so far; any real SNe Ia removed will be accounted for in the "effective visibility time" (§4) which is calculated using a Monte Carlo simulation.

3.3. *Typing*

We now use all available information about each candidate (spectroscopic confirmation, host galaxy redshift, all light curve information, as well as host galaxy luminosity and color) to classify each of the 60 remaining candidates as image artifact, active galactic nucleus (AGN), core-collapse SN (SN CC), or SN Ia.

3.3.1. *Image artifacts*

Although the automated selections were designed to eliminate image artifacts such as subtraction residuals and cosmic rays, they were made to be somewhat tolerant so that real SNe were not eliminated. The result is that some artifacts slip through. Candidates located close to the cores of relatively bright galaxies that show adjoining negative and positive areas in subtractions are likely to be caused by mis-alignment between the reference and search image. For such candidates, we inspected the full light curve for consistency with the general shape of a SN Ia light curve. For fourteen of these, the light curve is completely inconsistent with that of a SN Ia. Their light curves have either multiple peaks, long flat portions followed by one or two lower points, and/or i_{775} data that shows no change. We classify these fourteen candidates

as subtraction residuals with negligible classification uncertainty (very unlikely that any are SNe Ia).

Candidates where one or two of the four z_{850} exposures was clearly affected by a cosmic ray or hot pixel may be false detections. These can pass the automated cosmic ray rejection when they occur on a galaxy. For two such candidates, we used the lack of any change in the i_{775} light curve to rule out a SN Ia: fitting SN templates with a range of redshifts and extinctions resulted in observed i_{775} fluxes too low by 4σ or more, given the z_{850} increase. One other candidate, SCP06W50, is less certain. It was discovered in the last visit to the cluster, making it difficult to constrain a template light curve. There is clearly a hot pixel or cosmic ray in one z_{850} exposure, but there appears to be some excess flux in the other three exposures as well. Also, there is a point-source like detection in i_{775}, but offset $\sim$1.2 pixels from the z_{850} detection. While the i_{775} detection may also be a cosmic ray, it is possible that this candidate is a SN caught very early. The elliptical "host" galaxy was not observed spectroscopically, but we estimate its redshift to be $0.60 < z < 0.85$ based on the color of $i_{775} - z_{850} = 0.55$ and stellar population models of Bruzual & Charlot (2003, hereafter BC03).

Of the 17 total candidates classified as image artifacts, SCP06W50 is the only one with significant uncertainty. However, this uncertainty does not affect the cluster SN Ia rate as the host galaxy is clearly in the cluster foreground.

3.3.2. AGN

Candidates positioned directly on the cores of their host galaxies may be AGN. Four such candidates were spectroscopically confirmed as AGN: SCP06L22 ($z = 1.369$), SCP06V6 ($z = 0.903$) and SCP05X13 ($z = 1.642$) and SCP06U3 ($z = 1.534$). A fifth candidate, SCP06F3, is spectroscopically consistent with an AGN at $z = 1.21$, but is less certain (see spectroscopy reported in Morokuma et al. 2010). SCP06L22, SCP05X13, SCP06U3 and SCP06F3 also have light curves that are clearly inconsistent with SNe Ia (observer frame rise times of 100 days or more, or declining phases preceding rising phases). Of the "on core" candidates that were not observed spectroscopically, five exhibit light curves that decline before rising or have rise times of 100 days or more. A sixth candidate, SCP06Z51 exhibited slightly varying fluxes that could be due to either subtraction residuals or an AGN. However, its light curve is clearly inconsistent with a SN Ia, especially considering the apparent size, magnitude and color of the host galaxy. Summarizing, there are 11 "on-core" candidates certain not to be SNe Ia.

Three other "on-core" candidates are also considered likely AGN on the basis of their light curves: SCP06Z50, SCP06U50 and SCP06D51. These three candidates are shown in Fig. 3. SCP06Z50 (Fig. 3, top left), has a rise-fall behavior in the first three z_{850} observations of its light curve that *could* be consistent with a SN Ia light curve. However, given that the host galaxy is likely at $z \lesssim 1$ based on its magnitude and color, the SN would be fainter than a normal SN Ia by 1 magnitude or more. Considering the proximity to the galaxy core and the additional variability seen in the last two observations, SCP06Z50 is most likely an AGN. The light curve of candidate SCP06U50 (Fig. 3, top right) also exhibits a rise-fall that could be consistent with a supernova light curve. However, its host is morphologically elliptical and likely at $z \lesssim 0.7$ based on its color. At $z \lesssim 0.7$, a SN Ia would have to be very reddened ($E(B - V) \gtrsim 1$) to match the color and magnitude of the SCP06U50 light curve. As

this is very unlikely (considering that the elliptical host likely contains little dust), we conclude that SCP06U50 is also most likely an AGN. Finally, SCP06D51 (Fig. 3, bottom left) was discovered in the last visit, on the core of a spiral galaxy. We classify it as an AGN based on the earlier variability in the light curve. As these galaxies are all most likely in the cluster foregrounds, even the small uncertainty in these classifications is not a concern for the cluster rate calculation here.

Note that one of the candidates classified here as a clear AGN, SCP06U6, was reported as a SN with unknown redshift by Dawson09, due to the fact that spectroscopy revealed no evidence of an AGN. However, it is on the core of a compact galaxy, and has a clear $\gtrsim 100$ day rise in both z_{850} and i_{775} (Fig. 3, bottom right). While it could possibly be a very peculiar SN with a long rise time, what is important for this analysis is that it is clearly not a SN Ia.

3.3.3. Supernovae

After removing 17 image artifacts and 14 AGN, 29 candidates remain (listed in Table 3). One of these is the peculiar transient SCP 06F6 (also known as SN SCP06F6) reported by Barbary et al. (2009). Various explanations have been considered by, e.g., Gänsicke et al. (2009), Soker et al. (2010) and Chatzopoulos et al. (2009). It appears that SCP 06F6 may be a rare type of supernova, with redshift $z = 1.189$ (Quimby et al. 2009). While its precise explanation is still uncertain, SCP 06F6 is clearly not a SN Ia, so we don't consider it further here.

Note that Table 3 contains 10 fewer candidates than the list presented by Dawson09. This is unsurprising; here we have intentionally used a stricter selection than in the original search, the source for the Dawson09 sample. Still, after finalizing our selection method we checked that there were no unexpected discrepancies. Five of the Dawson09 candidates (SCP06B4, SCP06U2, SCP06X18, SCP06Q31, SCP06T1) fell just below either the detection or signal-to-noise thresholds in our selection. These were found in the original search because detection thresholds were set slightly lower, and because the images were sometimes searched in several different ways. For example, in the original search SCP06B4 was only found by searching an i_{775} subtraction. Two Dawson09 candidates (SCP05D55, SCP06Z52) were found too far on the decline and failed the light curve requirements (§3.2). Three Dawson09 candidates (SCP06X27, SCP06Z13, SCP06Z53) were found while searching in "follow-up" visits, which were not searched here. SCP06U6 passed all requirements, but is classified here as an AGN, as noted above. With the exception of SCP06U6, all of these candidates are likely to be supernovae (mostly core collapse). However, the types of candidates that did not pass our requirements are not of concern for this analysis. Finally, SCP06M50 was not reported in Dawson09, but is classified here as a SN, although a highly uncertain one (discussed in detail in §3.3.4).

Thanks to the extensive ground-based spectroscopic followup campaign, we were able to obtain spectroscopic redshifts for 25 of the 29 SNe. The redshift reported in Table 3 is derived from the SN host galaxy for all but one candidate (SCP06C1) where the redshift is from the SN spectrum itself. Of the 25 candidates with redshifts, eight are in clusters and 17 are in the field. Note that this high spectroscopic completeness is particularly important for determining the cluster or non-cluster status of each SN, which directly affects the determination of the cluster SN Ia rate. The possible cluster memberships of the four candidates lacking redshifts are
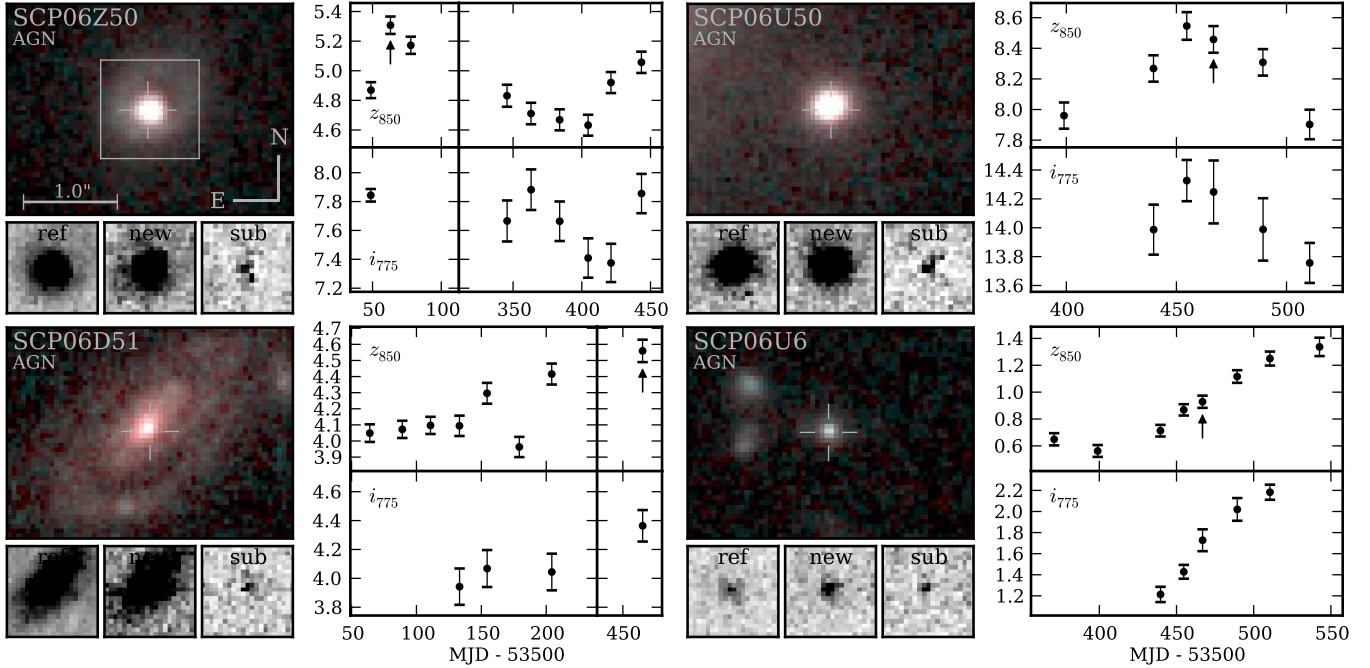
Figure 3. Images and light curves of four of the 14 candidates classified as AGN. For each candidate, the upper left panel shows the two-color stacked image (i_{775} and z_{850}) of the host galaxy, with the position of the transient indicated. The three smaller panels below the stacked image show the reference, new, and subtracted images for the discovery visit. The right panel shows the light curve at the SN position (including host galaxy light) in the z_{850} (*top*) and i_{775} (*bottom*) bands. The y axes have units of counts per second in a 3 pixel radius aperture. The effective zeropoints are 23.94 and 25.02 for z_{850} and i_{775}, respectively. The discovery visit is indicated with an arrow in the z_{850} plot.

discussed below.

We determine the type of each of the 29 supernovae using a combination of methods in order to take into account all available information for each supernova. This includes (a) spectroscopic confirmation, (b) the host galaxy environment, and (c) the SN light curve. To qualify the confidence of each supernova's type, we rank the type as "secure," "probable," or "plausible":

Secure SN Ia: Has spectroscopic confirmation or *both* of the following: (1) an early-type host galaxy with no recent star formation and (2) a light curve with shape, color and magnitude consistent with SNe Ia and inconsistent with other types.

Probable SN Ia: Fulfills either the host galaxy requirement or the light curve requirement, but not both.

Plausible SN Ia: The light curve is indicative of a SN Ia, but there is not enough data to rule out other types.

Secure SN CC: Has spectroscopic confirmation (note that there are no such candidates in this sample).

Probable SN CC: The light curve is consistent with a core-collapse SN and inconsistent with a SN Ia.

Plausible SN CC: Has a light curve indicative of a core-collapse SN, but not inconsistent with a SN Ia.

This ranking system is largely comparable to the "gold," "silver," "bronze" ranking system of Strolger et al. (2004), except that we do not use their "UV deficit" criterion. This is because our data do not include the bluer F606W filter, and because SNe Ia and CC are only distinct in UV flux for a relatively small window early in the light curve. Below, we discuss in detail the three typing methods used.

(a) Spectroscopic confirmation: During the survey, seven candidates were spectroscopically confirmed as SNe Ia (Dawson09, Morokuma et al. 2010). These seven (three of which are in clusters) are designated with an "a" in the "typing" column of Table 3. All seven candidates have a light curve shape, absolute magnitude and color consistent with a SN Ia. Although the spectroscopic typing by itself has some degree of uncertainty, the corroborating evidence from the light curve makes these "secure" SNe Ia.

(b) Early-type host galaxy: The progenitors of core-collapse SNe are massive stars ($> 8 M_\odot$) with main sequence lifetimes of < 40 Myr. Thus, core-collapse SNe only occur in galaxies with recent star formation. Early-type galaxies, having typically long ceased star formation, overwhelmingly host Type Ia SNe (e.g., Cappellaro et al. 1999; Hamuy et al. 2000). In fact, in an extensive literature survey of core-collapse SNe reported in early-type hosts, Hakobyan et al. (2008) found that only three core-collapse SNe have been recorded in early-type hosts, and that the three host galaxies in question had either undergone a recent merger or were actively interacting. In all three cases there are independent indicators of recent star formation. Therefore, in the cases where the host galaxy morphology, photometric color, and spectrum all indicate an early-type galaxy with no signs of recent star formation or interaction, we can be extremely confident that the SN type is Ia. These cases are designated by a "b" in the "typing" column of Table 3. We emphasize that in all of these cases, spectroscopy reveals no signs of recent star formation and there are no visual or morphological signs of interaction. (See Meyers10 for detailed studies of these SN host galaxy properties.)

(c) Light curve: SNe Ia can be distinguished from most common types of SNe CC by some combination of light curve shape, color, and absolute magnitude. We compare the light curve of each candidate to template light curves for SN Ia

Table 3
Supernovae

ID	Nickname	R.A. (J2000)	Decl. (J2000)	z	SN Type	Confidence	Typing
Cluster Members							
SN SCP06C1	Midge	$12^h 29^m 33^s.012$	$+01° 51' 36''.67$	0.98	Ia	secure	a,c
SN SCP05D0	Frida	$02^h 21^m 42^s.066$	$-03° 21' 53''.12$	1.014	Ia	secure	a,b,c
SN SCP06F12	Caleb	$14^h 32^m 28^s.748$	$+33° 32' 10''.05$	1.11	Ia	probable	c
SN SCP06H5	Emma	$14^h 34^m 30^s.139$	$+34° 26' 57''.29$	1.231	Ia	secure	b,c
SN SCP06K18	Alexander	$14^h 38^m 10^s.663$	$+34° 12' 47''.19$	1.412	Ia	probable	b
SN SCP06K0	Tomo	$14^h 38^m 08^s.366$	$+34° 14' 18''.08$	1.416	Ia	secure	b,c
SN SCP06R12	Jennie	$02^h 23^m 00^s.082$	$-04° 36' 03''.04$	1.212	Ia	secure	b,c
SN SCP06U4	Julia	$23^h 45^m 29^s.429$	$-36° 32' 45''.73$	1.05	Ia	secure	a,c
Cluster Membership Uncertain							
SN SCP06E12	Ashley	$14^h 15^m 08^s.141$	$+36° 12' 42''.94$	$\cdots$	Ia	plausible	c
SN SCP06N32	$\cdots$	$02^h 20^m 52^s.368$	$-03° 34' 13''.32$	$\cdots$	CC	plausible	c
Not Cluster Members							
SN SCP06A4	Aki	$22^h 16^m 01^s.077$	$-17° 37' 22''.09$	1.193	Ia	probable	c
SN SCP06B3	Isabella	$22^h 05^m 50^s.402$	$-01° 59' 13''.34$	0.743	CC	probable	c
SN SCP06C0	Noa	$12^h 29^m 25^s.654$	$+01° 50' 56''.58$	1.092	Ia	secure	b,c
SN SCP06C7	$\cdots$	$12^h 29^m 36^s.517$	$+01° 52' 31''.47$	0.61	CC	probable	c
SN SCP05D6	Maggie	$02^h 21^m 46^s.484$	$-03° 22' 56''.18$	1.314	Ia	secure	b,c
SN SCP06F6	$\cdots$	$14^h 32^m 27^s.394$	$+33° 32' 24''.83$	1.189	non-Ia	secure	a
SN SCP06F8	Ayako	$14^h 32^m 24^s.525$	$+33° 33' 50''.75$	0.789	CC	probable	c
SN SCP06G3	Brian	$14^h 29^m 28^s.430$	$+34° 37' 23''.13$	0.962	Ia	plausible	c
SN SCP06G4	Shaya	$14^h 29^m 18^s.743$	$+34° 38' 37''.38$	1.35	Ia	secure	a,b,c
SN SCP06H3	Elizabeth	$14^h 34^m 28^s.879$	$+34° 27' 26''.61$	0.85	Ia	secure	a,c
SN SCP06L21	$\cdots$	$14^h 33^m 58^s.990$	$+33° 25' 04''.21$	$\cdots$	CC	plausible	c
SN SCP06M50	$\cdots$	$16^h 04^m 25^s.300$	$+43° 04' 51''.85$	$\cdots$	$\cdots$	$\cdots$	$\cdots$
SN SCP05N10	Tobias	$02^h 20^m 52^s.878$	$-03° 33' 40''.20$	0.203	CC	plausible	c
SN SCP06N33	Naima	$02^h 20^m 57^s.699$	$-03° 33' 23''.97$	1.188	Ia	probable	c
SN SCP05P1	Gabe	$03^h 37^m 50^s.352$	$-28° 43' 02''.66$	0.926	Ia	probable	c
SN SCP05P9	Lauren	$03^h 37^m 44^s.512$	$-28° 43' 54''.58$	0.821	Ia	secure	a,c
SN SCP06U7	Ingvar	$23^h 45^m 33^s.867$	$-36° 32' 43''.48$	0.892	CC	probable	c
SN SCP06X26	Joe	$09^h 10^m 37^s.889$	$+54° 22' 29''.07$	1.44	Ia	plausible	c
SN SCP06Z5	Adrian	$22^h 35^m 24^s.966$	$-25° 57' 09''.61$	0.623	Ia	secure	a,c

Note. — Typing: (a) Spectroscopic confirmation. (b) Host is morphologically early-type, with no signs of recent star formation. (c) Light curve shape, color, magnitude consistent with type. We do not assign a type for SCP06M50 because there is significant uncertainty that the candidate is a SN at all.

and various SN CC subtypes to test if the candidate could be a SN Ia or a SN CC. For candidates lacking both spectroscopic confirmation and an elliptical host galaxy, if there is sufficient light curve data to rule out all SN CC subtypes, the candidate is considered a "probable" SN Ia. If SN Ia can be ruled out, it is considered a "probable" SN CC. If neither SN Ia nor SN CC can be ruled out, the candidate is considered a "plausible" SN Ia or SN CC based on how typical the candidate's absolute magnitude and/or color would be of each type. This approach can be viewed as a qualitative version of the pseudo-Bayesian light curve typing approaches of, e.g., Kuznetsova & Connolly (2007); Kuznetsova et al. (2008); Poznanski et al. (2007a,b). SNe classified as "probable" here would likely have a Bayesian posterior probability approaching 1, while "plausible" SNe would have an intermediate probability (likely between 0.5 and 1.0). We consciously avoid the full Bayesian typing approach because it can obscure large uncertainties in the priors such as luminosity distributions, relative rates, light curve shapes, and SN subtype fractions. Also, the majority of our candidates have more available light curve information than those of Kuznetsova et al. (2008) and Poznanski et al. (2007b), making a calculation of precise classification uncertainty less necessary. In general, classification uncertainty from light curve

fitting is not a concern for the cluster rate calculation as most cluster-member candidates are securely typed using methods (a) and/or (b), above. It is more of a concern for the volumetric field rate calculation based on the non-cluster candidates (Barbary et al., in preparation), though the uncertainty in the field rate is still dominated by Poisson error.

For each candidate we fit template light curves for SN Ia, Ibc, II-P, II-L, and IIn. We use absolute magnitude and color as a discriminant by limiting the allowed fit ranges according to the known distributions for each subtype. For SN Ia we start with the spectral time series template of Hsiao et al. (2007), while for the core-collapse types we use templates of Nugent et al. (2002)[28]. Each spectral time series is redshifted to the candidate redshift and warped according to the desired color. Observer-frame template light curves are then generated by synthetic photometry in the i_{775} and z_{850} filters. The magnitude, color, date of maximum light, and galaxy flux in i_{775} and z_{850} are allowed to vary to fit the light curve data. For the SN Ia template, the linear timescale or "stretch" (e.g., Perlmutter et al. 1997; Guy et al. 2005) is also allowed to vary within the range $0.6 < s < 1.3$. We constrain the absolute magnitude for each subtype to the range observed by

[28] See http://supernova.lbl.gov/~nugent/nugent_templates.html.

Table 4
SN light curve template parameter ranges

SN type	Template	Observed M_B	$E(B-V)$	s
Ia	Hsiao	$-17.5 - -20.1$	$-0.2 - 0.6$	$0.6 - 1.3$
Ibc	Nugent	$-15.5 - -18.5$	$-0.1 - 0.5$	1.0
II-L	Nugent	$-16.0 - -19.0$	$-0.1 - 0.5$	1.0
II-P	Nugent	$-15.5 - -18.0$	$-0.1 - 0.5$	1.0
IIn	Nugent	$-15.5 - -19.1$	$-0.1 - 0.5$	1.0

Li et al. (2010); Our allowed range fully encompasses their observed luminosity functions (uncorrected for extinction) for a magnitude-limited survey for each subtype. We correct from their assumed value of $H_0 = 73$ km s^{-1} Mpc^{-1} to our assumed value of $H_0 = 70$ km s^{-1} Mpc^{-1} and K-correct from R to B band. To avoid placing too strict of an upper limit on SN CC brightness, we use the bluest maximum-light spectrum available when K-correcting (e.g., for SN Ibc we use a bluer spectrum than that of Nugent et al. (2002), as bluer SNe Ibc have been observed). The resulting allowed M_B range for each subtype is shown in Table 4. Note that the range for Ibc does not include ultra-luminous SNe Ic (such as those in the luminosity functions of Richardson et al. (2002)) as none were discovered by Li et al. (2010). While such SNe can mimic a SN Ia photometrically, the Li et al. (2010) results indicate that they are intrinsically rare, and even Richardson et al. (2002) show that they make up at most $\sim$20% of all SNe Ibc. Still, we keep in mind that even candidates compatible only with our SN Ia template and incompatible with SN CC templates may in fact be ultra-luminous SNe Ic, though the probability is low. This is why any candidate typed based on light curve alone has a confidence of at most "probable," rather than "secure." The allowed ranges of "extinction," $E(B-V)$, are also shown in Table 4. For SN Ia, $E(B-V)$ is the difference in $B-V$ color from the Hsiao et al. (2007) template. As the observed distribution of SNe includes SNe bluer than this template, SNe Ia as blue as $E(B-V) = -0.2$ are allowed. Given an $E(B-V)$, the spectral template is warped according to the SALT color law (Guy et al. 2005), with an effective $R_B = 2.28$ (Kowalski et al. 2008). For SN CC templates, extinction as low as $E(B-V) = -0.1$ is allowed to reflect the possibility of SNe that are intrinsically bluer than the Nugent et al. (2002) templates. Templates are then warped using a Cardelli et al. (1989) law with $R_B = 4.1$. Extinctions are limited to $E(B-V) < 0.5$ (implying an extinction of $A_B \sim 2$ magnitudes for SNe CC).

The light curve template with the largest χ^2 P-value is generally taken as the type. We also evaluate each fit by eye to check that the best-fit template adequately describes the light curve. Figure 4 shows the best-fit template for each candidate. For candidates typed on the basis of spectroscopic confirmation or an elliptical host galaxy only the SN Ia template is shown. For candidates typed on the basis of the light curve alone, we show both the best-fit SN Ia and best-fit SN CC templates for comparison. The confidence in the best-fit template is either "probable" or "plausible" depending on how well other templates fit: If the next-best fit has a P-value that is smaller than $10^{-3} \times P_{\text{best}}$, the best-fit template is considered the only acceptable fit and the confidence is "probable." If the next-best fit has a P-value larger than $10^{-3} \times P_{\text{best}}$ the confidence is "plausible." Finally, note that the photometry used here is simple aperture photometry with fixed aperture corrections. For SN Ia cosmology we use color-dependent

aperture corrections, as described in Suzuki et al. (in preparation).

3.3.4. *Comments on individual SN light curves*

Here we comment in greater detail on a selection of individual candidates, particularly those with the greatest uncertainty in typing. For each candidate, see the corresponding panel of Fig. 4 for an illustration of the candidate host galaxy and light curve.

SN SCP06E12. We were unable to obtain a host galaxy redshift due to the faintness of the host. The color of the host galaxy is consistent with the cluster red sequence. The candidate light curve is consistent with a SN Ia at the cluster redshift of $z = 1.03$, but is also consistent with SN II-L at $z = 1.03$. Different SN types provide an acceptable fit over a fairly wide range of redshifts. As the SN Ia template provides a good fit with typical parameters, we classify the candidate as a "plausible" SN Ia. However, there is considerable uncertainty due to the uncertain redshift.

SN SCP06N32 also lacks a host galaxy redshift. If the cluster redshift of $z = 1.03$ is assumed, the candidate light curve is best fit by a SN Ibc template. A SN Ia template also yields an acceptable fit, but requires an unusually red color of $E(B-V) \sim 0.6$. Given the best-fit s and M_B values, the candidate would have an unusually large Hubble diagram residual of approximately -0.8 magnitudes. If the redshift is allowed to float, a SN Ia template with more typical parameters provides an acceptable fit at $z = 1.3$. A SN Ibc template still provides a better fit, with the best fit redshift being $z \sim 0.9$. As SN Ibc provides a better fit in both cases, we classify this as a "plausible" SN CC. However, there is considerable uncertainty in both the type and cluster membership of this candidate.

SN SCP06A4. We note that this candidate was observed spectroscopically, as reported in Dawson09. While the spectrum was consistent with a SN Ia, there was not enough evidence to definitely assign a type. The host galaxy is morphologically and photometrically consistent with an early-type galaxy, but there is detected [OII], a possible indication of star formation. We therefore rely on light curve typing for this candidate, assigning a confidence of "probable" rather than "secure."

SN SCP06G3 has only sparse light curve coverage. The best fit template is a SN Ia with $s = 1.3$, $E(B-V) = 0.3$ and $M_B = -18.5$, although these parameters are poorly constrained. A large stretch and red color would not be surprising given the spiral nature of the host galaxy. It is also consistent with a II-L template, although the best fit color is unusually blue: $E(B-V) = -0.1$. Given that SN Ia yields more "typical" fit parameters and that, at $z \sim 1$ a detected SN is more likely to be Type Ia than II, we classify this as a "plausible" Type Ia, with considerable uncertainty in the type.

SN SCP06L21 lacks a spectroscopic redshift, but has a distinct slowly-declining light curve that rules out a $z > 0.6$ SN Ia light curve. Even the best-fit Ia template at $z = 0.55$, shown in Fig. 4), is unusually dim ($M_B \approx -17.5$), making it unlikely that the candidate is a lower-redshift SN Ia. The light curve is better fit by a SN II-P template (with the best-fit redshift being $z = 0.65$). We therefore classify the candidate as a "probable" SN CC.

SN SCP06M50 is the most questionable "SN" candidate, having no obvious i_{775} counterpart to the increase seen in z_{850}. It may in fact be an image artifact or AGN. However, it appears to be off the core of the galaxy by $\sim$2 pixels (mak-
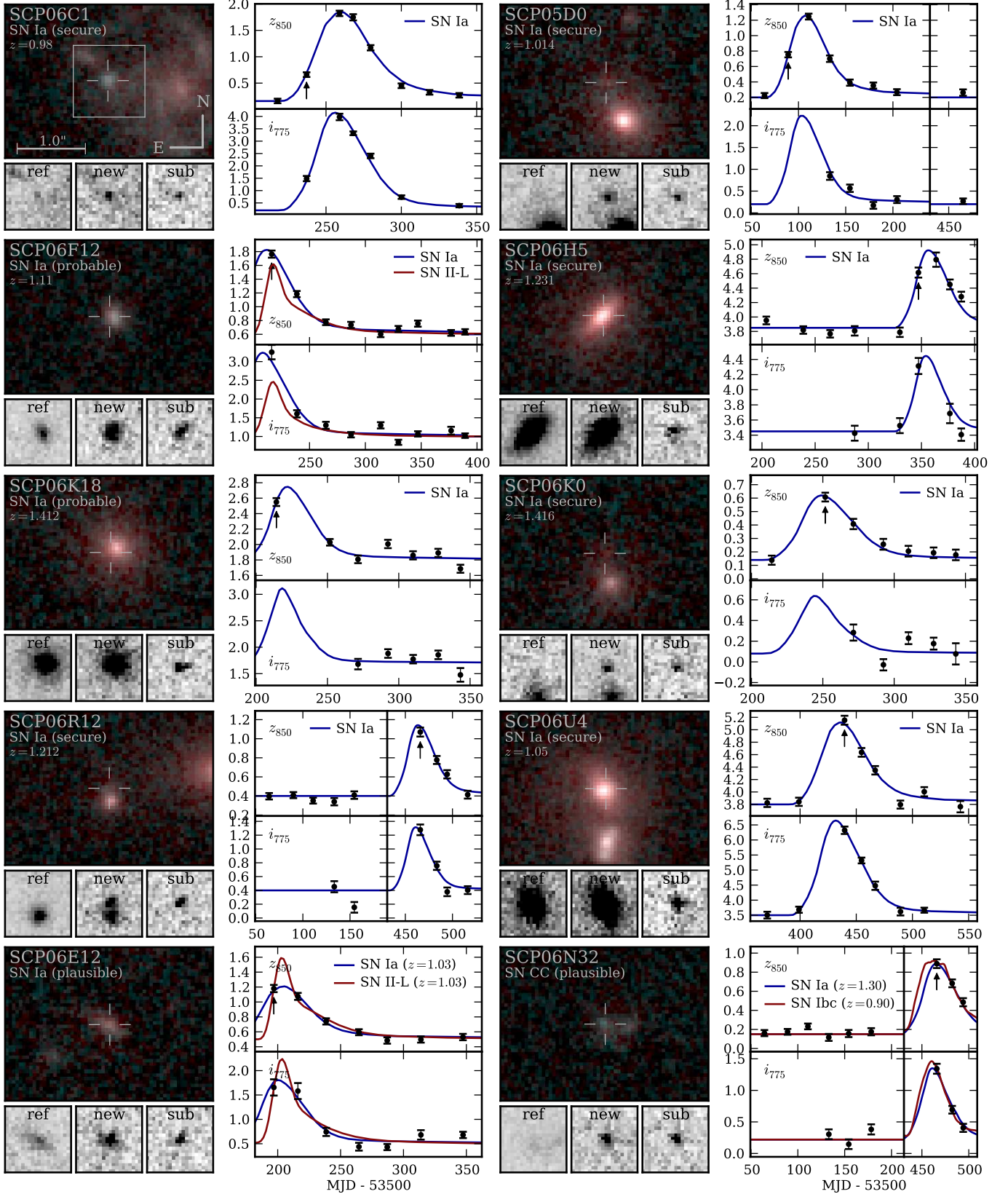
Figure 4. Images and light curves of the 29 candidates classified as supernovae. For each candidate, the upper left panel shows the 2-color stacked image (i_{775} and z_{850}) of the supernova host galaxy, with the SN position indicated. The three smaller panels below the stacked image show the reference, new, and subtracted images for the discovery visit. The right panel shows the light curve at the SN position (including host galaxy light) in the z_{850} (*top*) and i_{775} (*bottom*) bands. The y axes have units of counts per second in a 3 pixel radius aperture. The effective zeropoints are 23.94 and 25.02 for z_{850} and i_{775}, respectively. The discovery visit is indicated with an arrow in the z_{850} plot. The best-fit SN Ia template is shown in blue. For cases where the type is SN Ia based on spectroscopic confirmation or host galaxy environment, only the best-fit SN Ia template is shown, to demonstrate the consistency of the light curve with the designation. For cases where the type is based only on the light curve fit, the best-fit core collapse SN template is shown in red. Note that the photometry used here is simple aperture photometry with fixed aperture corrections. For SN Ia cosmology we use color-dependent aperture corrections, as described in Suzuki et al. (in preparation).
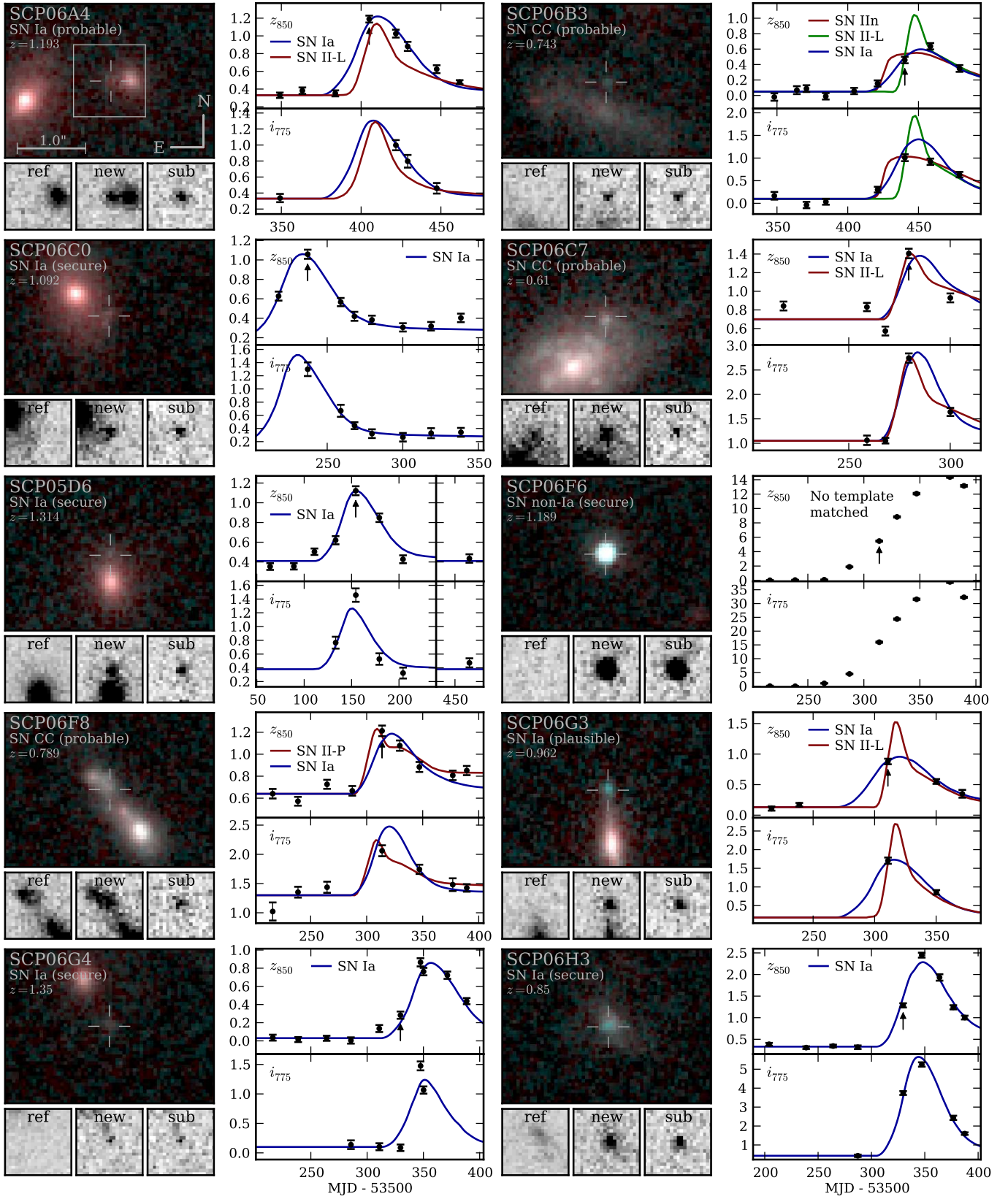
Figure 4. *Continued*
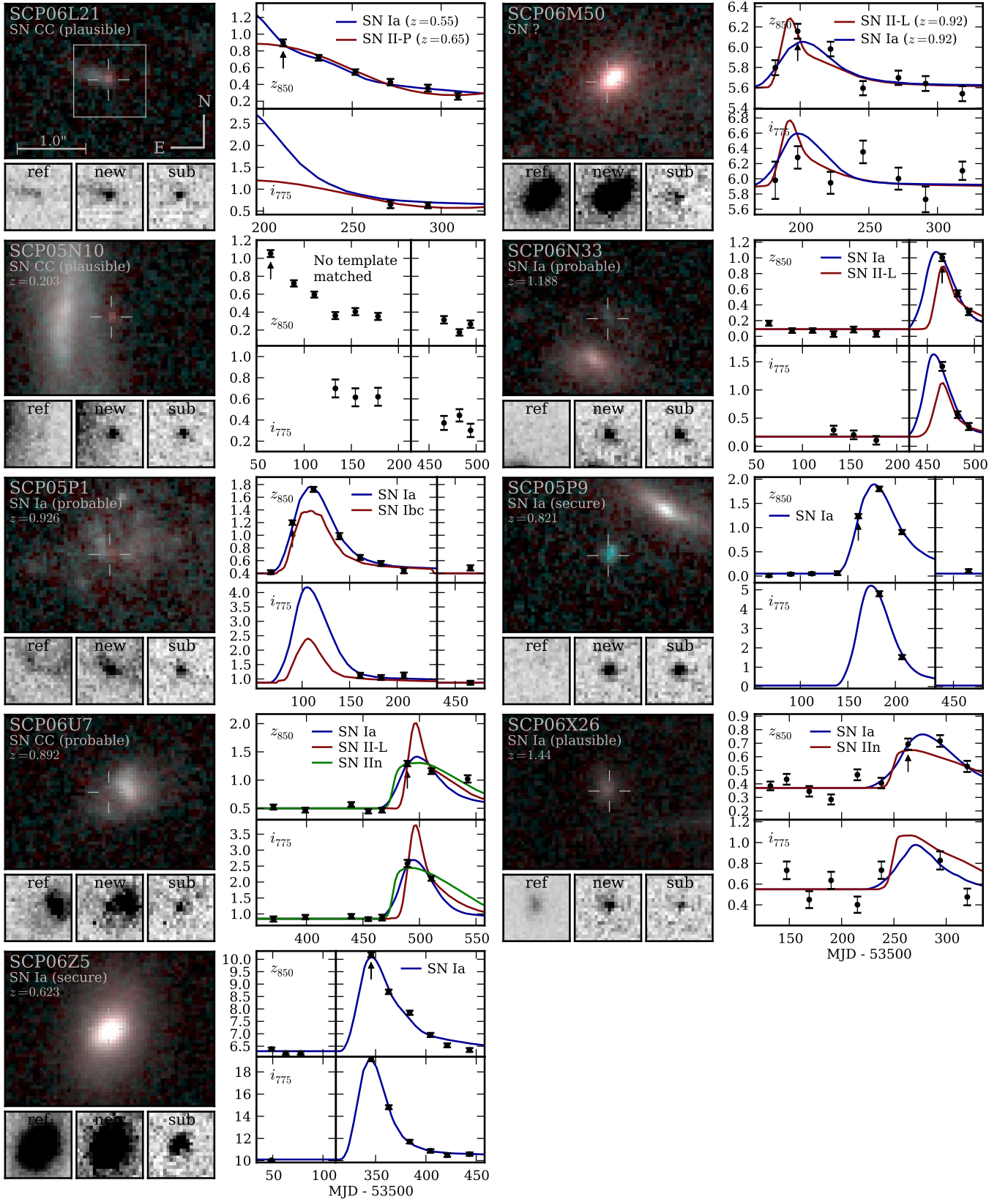
Figure 4. *Continued*

ing AGN a less likely explanation), and shows an increase in z_{850} flux in two consecutive visits, with no obvious cosmic rays or hot pixels (making an image artifact less likely as well). The galaxy is likely to be a cluster member: its color and magnitude put it on the cluster red sequence, it is morphologically early-type, and it is only $19''$ from the cluster center. Under the assumption that the candidate is a supernova and at the cluster redshift of $z = 0.92$, no template provides a good fit due to the lack of an i_{775} detection and the constraints on $E(B - V)$. In particular, a SN Ia template would require $E(B - V) > 0.6$. (The best-fit template shown in Fig. 4 is with $E(B - V) = 0.6$.) If the redshift is allowed to float, it is possible to obtain a good fit at higher redshift ($z \sim 1.3$), but still with $E(B - V) \gtrsim 0.4$, regardless of the template type. Given the color and early-type morphology of the host galaxy, it is unlikely to contain much dust. There is thus no consistent picture of this candidate as a SN, and we do not assign a type. However, note that the candidate is unlikely to be a cluster SN Ia.

SN SCP05N10 is the lowest-redshift SN candidate in our sample at $z = 0.203$. Its light curve shape is inconsistent with a SN Ia occurring well before the first observation, and its luminosity is too low for a SN Ia with maximum only slightly before the first observation. Therefore, we call this a "probable" SN CC. For all SN types, the best fit requires maximum light to occur well before the first observation, making all fits poorly constrained.

SN SCP06X26 has a tentative redshift of $z = 1.44$, derived from a possible [OII] emission line in its host galaxy. Given this redshift, a Ia template provides an acceptable fit, consistent with a typical SN Ia luminosity and color. However, we consider this a "plausible," rather than "probable, " SN Ia, given the uncertain redshift and low signal-to-noise of the light curve data.

3.4. *Summary*

In the previous section we addressed the type of all 29 candidates thought to be SNe. However only the cluster-member SNe Ia are of interest for the remainder of this paper. There are six "secure" cluster-member SNe Ia, and two "probable" SNe Ia, for a total of eight. In addition, SCP06E12 is a "plausible" SN Ia and may be a cluster member. Two other candidates, SCP06N32 and SCP06M50, cannot be definitively ruled out as cluster-member SNe Ia, but are quite unlikely for reasons outlined above. We take eight cluster SNe Ia as the most likely total. It is unlikely that *both* of the "probable" SNe Ia are in fact SNe CC. We therefore assign a classification error of $^{+0.0}_{-0.5}$ for each of these, resulting in a lower limit of seven cluster-member SNe Ia. There is a good chance that SCP06E12 is a cluster-member SN Ia, while there is only a small chance that SCP06N32 and SCP06M50 are either cluster SNe Ia. For these three candidates together, we assign a classification error of $^{+1}_{-0}$, for an upper limit of nine. Thus, 8 ± 1 is the total number of observed cluster SNe Ia.

4. EFFECTIVE VISIBILITY TIME

With a systematically selected SN Ia sample now in hand, the cluster SN Ia rate is given by

$$\mathcal{R} = \frac{N_{\text{SN Ia}}}{\sum_j T_j L_j}, \tag{1}$$

where $N_{\text{SN Ia}}$ is the total number of SNe Ia observed in clusters in the survey, and the denominator is the total effective time-luminosity for which the survey is sensitive to SNe Ia in clusters. j denotes the cluster. L_j is the luminosity of cluster j visible to the survey in a given band. T_j is the "effective visibility time" (also known as the "control time") for cluster j. This is the effective time for which the survey is sensitive to detecting a SN Ia, calculated by integrating the probability of detecting a SN Ia as a function of time over the span of the survey. It depends on the redshift of the SN Ia to be detected and the dates and depths of the survey observations. As each cluster has a different redshift and different observations, the control time is determined separately for each cluster. To calculate a rate per stellar mass, L_j is replaced by M_j.

Equation (1) is for the case where the entire observed area for each cluster is observed uniformly, yielding a control time T that applies to the entire area. In practice, different areas of each cluster may have different observation dates and/or depths, resulting in a control time that varies with position. This is particularly true for this survey, due to the rotation of the observed field between visits and the gap between ACS chips. Therefore, we calculate the control time as a function of position in each observed field, $T_j(x, y)$. As the cluster luminosity is also a function of position, we weight the control time at each position by the luminosity at that position. In other words, we make the substitution

$$T_j L_j \Rightarrow \int_{x,y} T_j(x, y) L_j(x, y). \tag{2}$$

The effective visibility time T at a position (x, y) on the sky is given by

$$T(x, y) = \int_{t=-\infty}^{t=\infty} \eta^*(x, y, t) \epsilon(x, y, t) dt. \tag{3}$$

The integrand here is simply the probability for the survey and our selection method to detect (and keep) a SN Ia at the cluster redshift that explodes at time t, and position (x, y). This probability is split into the probability η^* of detecting the supernova and the probability ϵ that the supernova passes all "light curve" cuts. As each SN has multiple chances for detection, the total probability of detection η^* is a combination of the probabilities of detection in each observation. For example, if we have two search visits at position (x, y), $\eta^*(t)$ is given by

$$\eta^*(t) = \eta_1(t) + (1 - \eta_1(t))\eta_2(t), \tag{4}$$

where $\eta_i(t)$ is the probability of detecting a SN Ia exploding at time t in visit i. In other words, the total probability of finding the SN Ia exploding at time t is the probability of finding it in visit 1 plus the probability that it was *not* found in visit 1 times the probability of finding it in visit 2. This can be generalized to many search visits: The contribution of each additional visit to the total probability is the probability of not finding the SN in any previous visit times the probability of finding the SN in that visit.

In practice, we calculate $T(x, y)$ in two steps: First, we determine the probability η of detecting a new point source in a single image as a function of the point source magnitude. This is discussed in §4.1. Second, for each (x, y) position in the observed area we simulate a variety of SN Ia light curves at the cluster redshift occurring at various times during the survey. By considering the dates of the observations made during the survey at that specific position, we calculate the brightness and significance each simulated SN Ia would have in each z_{850} and i_{775} image. We then use our calculation of

η as a function of magnitude to convert the observed brightness into a probability of detecting the simulated SN in each observation. The light curve simulation is discussed in §4.2. The calculation of cluster luminosities, $L_j(x, y)$, is discussed in §5.

4.1. *Detection Efficiency Versus Magnitude*

Here we calculate the probability of detecting a new point source as a function of magnitude in a single subtraction. We use a Monte Carlo simulation in which artificial point sources of various magnitudes are added to each of the individual exposure images from the survey, before they are combined using MULTIDRIZZLE. Starting from the individual exposures allows us to test both the efficiency of the MULTIDRIZZLE process and our cosmic ray rejection (which uses the flux observed in the individual exposures). The point sources are placed on galaxies in positions that follow the distribution of light in each galaxy. Poisson noise is added to each pixel in the point source. The altered images are then run through the full image reduction and SN detection pipeline used in the search, and flagged candidates are compared to the input point sources.

We parameterize the detection efficiency by the ratio of point source flux to sky noise. This is a good choice because, in most cases, the detection efficiency will depend only on the contrast between the point source and the sky noise. However, there is an additional dependence on the surface brightness at the location of the point source: point sources near the core of galaxies will have a lower detection efficiency due to additional Poisson noise from the galaxy. For $0.6 < z < 1.5$ galaxies, we estimate that only $\sim 10\%$ of SNe will fall on regions where galaxy Poisson noise is greater than the sky noise (assuming SNe follow the galaxy light distribution). Still, we take this effect into account by splitting our sample of artificial point sources into four bins in underlying surface brightness. The detection efficiency is calculated separately in each bin (Fig. 5, top left panel). The first two bins, $\mu > 22.0$ and $22.0 > \mu > 20.6$ mag arcsec^{-2}, correspond to lower surface brightnesses where sky noise is dominant. As expected, their efficiency curves are very similar. In the third and fourth bins, corresponding to higher surface brightness, the Poisson noise from the galaxy dominates the sky noise, and the efficiency drops as a result.

For reference, the distribution of sky noise in the subtractions is shown in Figure 5 (right panel). Nearly all the searched area has a sky noise level between 0.006 and 0.012 counts sec^{-1} pixel^{-1}. For a typical value of 0.008, we show the corresponding point source z_{850} magnitude on the top axis of the left panel.

We find that the efficiency curve in each bin is well-described by the function

$$\eta(x) = \begin{cases} \frac{1}{2}(1 + ae^{-bx})[\mathrm{erf}((x - c)/d_1) + 1], & x < c \\ \frac{1}{2}(1 + ae^{-bx})[\mathrm{erf}((x - c)/d_2) + 1], & x \geq c \end{cases}, \tag{5}$$

where x is the ratio of point source flux to sky noise, and a, b, c, d_1 and d_2 are free parameters. An error function is the curve one would expect with a constant cut and Gaussian noise, but we find that two different scales (d_1 and d_2) in the error function, as well as an additional exponential term, are necessary to describe the slow rise to $\eta = 1$ at large x. This slow rise is due to rarer occurrences, such as cosmic rays coinciding with new point sources. The fitted functions for the four bins are plotted in the top left of Figure 5 and reproduced

in the bottom left of the figure for comparison. We use these fitted functions to calculate the effective visibility time in the following section.

4.2. *Simulated Lightcurves*

We simulate SN Ia light curves with a distribution of shapes, colors and absolute magnitudes. We use the (original) SALT (Guy et al. 2005) prescription in which the diversity of SN Ia light curves is characterized as a two-parameter family with an additional intrinsic dispersion in luminosity. The two parameters are the linear timescale of the light curve ("stretch", s) and the $B - V$ color excess, c. For each simulated SN, s and c are randomly drawn from the distributions shown in Figure 6 (*solid lines*). The stretch distribution is based on the observed distribution in passive hosts (Fig. 6, *left panel, grey histogram*) in the first-year Supernova Legacy Survey (SNLS) sample (Sullivan et al. 2006). Similarly, the color distribution is based on the observed color distribution (Fig. 6, *right panel, grey histogram*) in the first-year SNLS sample (Astier et al. 2006). The absolute magnitude of each simulated SN is set to

$$M_B = -19.31 - \alpha(s - 1) + \beta c + I \tag{6}$$

where -19.31 is the magnitude of an $s = 1$, $c = 0$ SN Ia in our assumed cosmology (Astier et al. 2006), $\alpha = 1.24$, $\beta = 2.28$ (Kowalski et al. 2008), and I is an added "intrinsic dispersion", randomly drawn from a Gaussian distribution centered at zero with $\sigma = 0.15$ mag.

We have chosen distributions that represent as accurately as possible the full distribution of SNe Ia occurring in reality. However, note that the control time is not actually very sensitive to the assumed distributions. This is because, for the majority of cluster redshifts in the survey, the detection efficiency is close to 100% during the time of the survey. Supernovae would thus have to be significantly less luminous in order to change the detection efficiency significantly. In the following section §4.3 we quantify the effect on the control time arising from varying the assumed SN Ia properties and show that they are sub-dominant compared to the Poisson error in the number of SNe observed. All sources of systematic errors are also summarized in §6.2.

To generate the simulated light curves in the observed bands, we use the Hsiao et al. (2007) SN Ia spectral time series template. For each simulated SN, the spectral time series is warped to match the selected color c and redshifted to the cluster restframe. Light curves are generated in the observed i_{775} and z_{850} filters using synthetic photometry, and the time axis is scaled according to the chosen value of s.

For each cluster, we calculate $T(x, y)$ in bins of 50×50 pixels ($2''.5 \times 2''.5$). In each bin, we simulate 100 SN light curves at random positions within the bin. For each simulated SN light curve, we shift the light curve in time across the entire range of observations, starting with maximum light occurring 50 days before the first observation and ending with maximum light occurring 50 days after the last observation. For each step in time we get the z_{850} and i_{775} magnitude of the SN at every date of observation. From the sky noise maps, we know the noise at the position of the simulated SN in every image. Using the curves in Figure 5, we convert the SN flux-to-noise ratio to the probability of the SN being detected in each z_{850} exposure. (Each simulated SN is also assigned a host galaxy surface brightness chosen from a distribution, in addition to the randomly selected s, c and I parameters; we
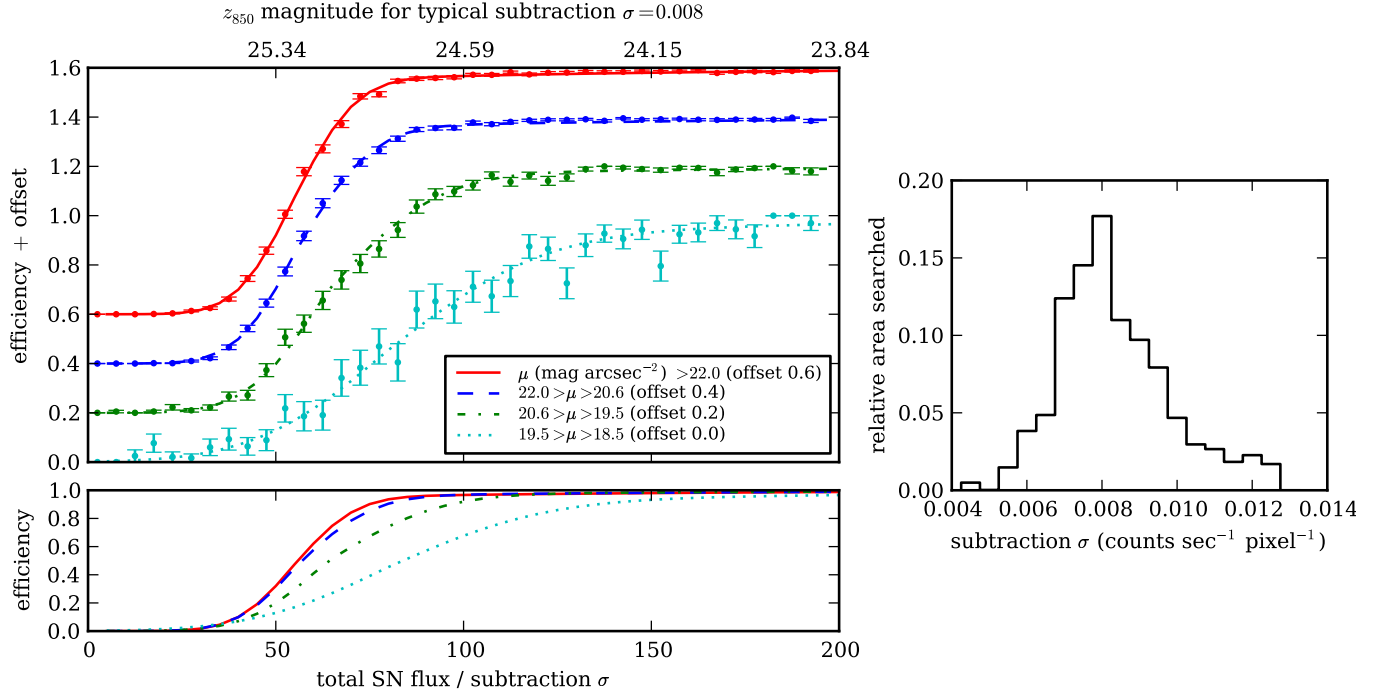
Figure 5. Point source detection efficiency in a single subtraction, as a function of the ratio of total point source flux to subtraction noise σ (counts sec^{-1} pixel^{-1}). The artificial point sources are split into four bins depending on the underlying galaxy surface brightness μ (mag arcsec^{-2}) at the point source position. The efficiency curve is calculated separately for each bin. In the upper left panel, the four bins are shown, offset for clarity. In the lower left panel, the fitted curves are reproduced without offset for comparison. Approximately 72,000 artificial point sources were used in total. The right panel shows the distribution of the noise level in the subtractions. The noise level differs by a factor of about two from the deepest to shallowest subtractions searched.
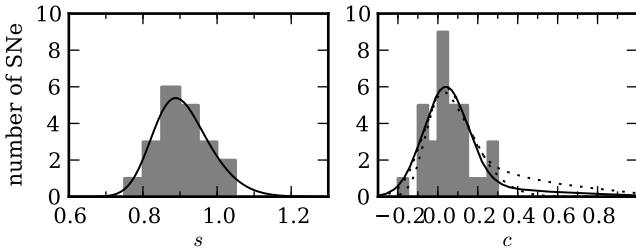
Figure 6. *Left panel:* stretch distribution used for simulated SNe (*solid line*) and the stretch distribution of first-year SNLS $z < 0.75$ SNe in passive hosts (Sullivan et al. 2006) (*grey histogram*). Note that the distribution is not changed significantly by cutting the sample at $z < 0.6$. Therefore we do not expect the sample to be significantly Malmquist biased. *Right panel:* color distribution of the first-year SNLS $z < 0.6$ SNe (Astier et al. 2006) (*grey histogram*) and the color distribution used for simulated SNe (*solid line*). The *dotted lines* show alternative color distributions used to assess the possible systematic error due to varying amounts of SNe being affected by dust.

use the Fig. 5 curve that corresponds to this surface brightness.) At the same time, we calculate the probability that the SN passes our light curve cuts (using both z_{850} and i_{775} simulated magnitudes). Multiplying these two probabilities gives the total probability of the simulated SN being included in the sample if it peaks at the given date. Integrating the probability over time (the entire range of dates) gives the control time for each simulated SN. We take the average control time of the 100 SNe as the value for the given bin. The resulting control time map, $T(x, y)$, therefore has a resolution of $2''.5 \times 2''.5$. $T(x, y)$ is shown for two example clusters in Figure 7.

4.3. *Effect of Varying SN Properties*

If the real distributions of SN Ia properties differs significantly from those assumed in our simulation, the $T(x, y)$

maps we have derived could misrepresent the true efficiency of the survey. Above we argued that the effect is likely to be small because the detection efficiency is close to 100% for most of the survey. Here we quantify the size of the possible effect on the control time by varying the assumed distributions.

To first order, changing the assumed distributions of s or c or changing the assumed spectral time series will affect the detection efficiency by increasing or decreasing the luminosity of the simulated SN. To jointly capture these effects, we shift the absolute magnitude of the simulated SNe Ia by $^{+0.2}_{-0.2}$ mag and recalculate the control times. To first order, this is equivalent to shifting the s distribution by $\Delta s = 0.2/\alpha \sim 0.16$ or shifting the c distribution by $\Delta c = 0.2/\beta \sim 0.09$. A -0.2 mag shift in absolute magnitude increases the control time, decreasing the inferred SN Ia rate by 6%. A $+0.2$ mag shift decreases the control time, increasing the SN Ia rate by 8%. These effects are sub-dominant compared to the Poisson error of $\gtrsim 30\%$ in the number of SNe observed. (Sources of error are summarized in §6.2 and Table 8.)

For the color distribution, in addition to a simple shift, we also quantify the effect of including a smaller or larger fraction of SNe significantly reddened by dust. In fact, we have good reasons to believe that most cluster SNe Ia will be in dust-free environments. A large fraction of the stellar mass in the clusters ($\sim 80\%$) is contained in red-sequence galaxies expected to have little or no dust. Our spectroscopic and photometric analysis (Meyers10) of the red-sequence galaxies confirms this expectation. Therefore, for our default c distribution (Fig. 6, right panel, solid line), we assumed that 20% of SNe (those occurring in galaxies not on the red sequence) could be affected by dust, and that the extinction of these SNe
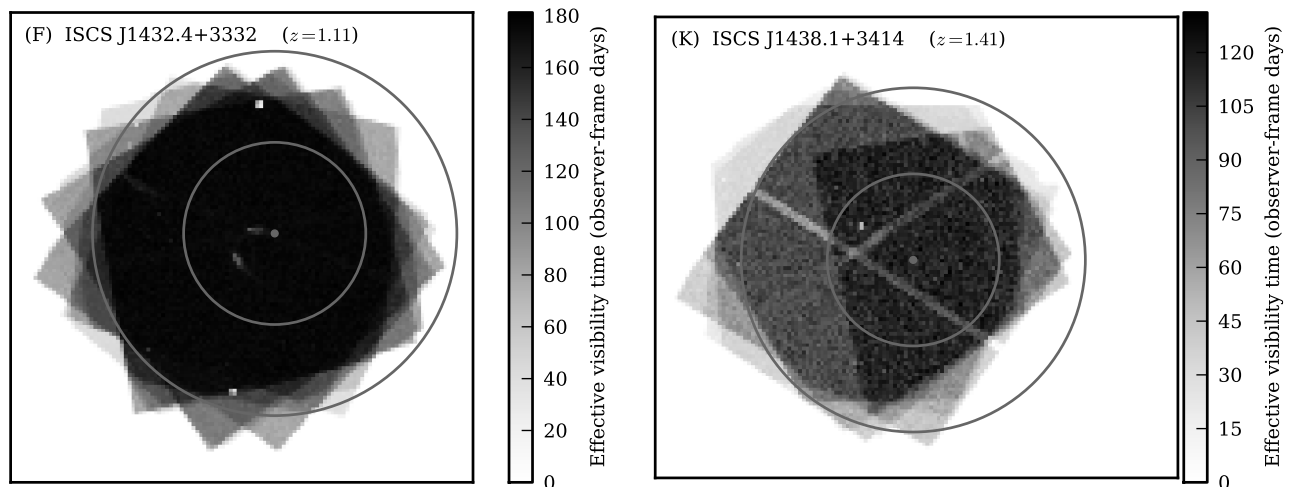
Figure 7. Example maps of effective visibility time for clusters ISCS J1432.4+3332 (F) and ISCS J1438.1+3414 (K). The dot denotes the cluster center and the inner and outer circles represent 0.5 Mpc and 1.0 Mpc radius, respectively. The "noise" in these maps is due to the finite number (100) of SNe simulated at each position. At lower redshift nearly all simulated SNe are recovered at each position, whereas at higher redshift a sizable fraction of simulated SNe are missed, resulting in a higher "noise" level.

would be distributed according to $P(A_V) \propto \exp(-A_V/0.33)$ [the inferred underlying A_V distribution of the SDSS-II sample (Kessler et al. 2009)]. All SNe are assumed to have an intrinsic dispersion in color to match the observed SNLS distribution at $c < 0.3$. It might be the case that even fewer SNe are affected by dust, or (unlikely) more SNe are affected by dust. As extreme examples, we tested two alternative distributions (dotted lines in Fig. 6). In the first, we assumed that the SNLS sample was complete and characterized the full c distribution, with a negligible number of $c > 0.4$ SNe. This increases the control time by only 2%. In the second, we increase the fraction of dust-affected SNe from 20% to 50%. Even though this alternative distribution includes an additional $\sim$30% more reddened SNe (unlikely to be true in reality), the average control time is only lower by 9% (increasing the rate by 10%). We use these values as the systematic error in the assumed dust distribution.

5. CLUSTER LUMINOSITIES AND MASSES

In this section, we calculate the total luminosity of each cluster and use the luminosity to infer a stellar mass. Only a small subset of galaxies in each field have known redshifts, making it impossible to cleanly separate cluster galaxies from field galaxies. Therefore, we use a "background subtraction" method to estimate cluster luminosities statistically: we sum the luminosity of all detected galaxies in the field and subtract the average "background luminosity" in a non-cluster field. To increase the significance, we discard from both measurements all galaxies brighter than the cD galaxy (or estimated BCG magnitude when there is no obvious cD galaxy). This approach follows that of Sharon et al. (2007). For the blank field, we use the GOODS[29] fields (Giavalisco et al. 2004) as they have similarly deep or deeper observations in both ACS i_{775} and z_{850}. We estimate cluster stellar masses based on the cluster luminosities and stellar mass-to-light ratios derived from stellar evolution models.

[29] Based on observations made with the NASA/ESA *Hubble Space Telescope*. The observations are associated with programs GO-9425, GO-9583 and GO-10189

5.1. *Galaxy Selection and Photometry*

We use the stacked i_{775} and z_{850} band images of each cluster, which have total exposure times in the range 1060 – 4450 seconds and 5440 – 16,935 seconds, respectively. Galaxy catalogs are created using the method described in detail by Meyers10: We run SEXTRACTOR (Bertin & Arnouts 1996) in dual-image mode using the z_{850} image for detection, and use a two-pass Cold/Hot method (Rix et al. 2004) to optimally de-blend galaxies. We remove stars from the catalog based on the CLASS_STAR and FLUX_RADIUS parameters from the z_{850} image.

It is notoriously difficult to determine accurate total fluxes for extended sources. However, as we are only concerned with the summed flux of many galaxies, it is not important that the estimate be accurate for each individual galaxy, only that the estimate is unbiased in the aggregate. We use the SEXTRACTOR MAG_AUTO photometry (which gives the total flux within a flexible elliptical aperture) and apply a correction determined using the Monte Carlo simulation described below. In order to make the aperture correction as small as possible, we use a relatively large "Kron factor" of 5.0, meaning that the MAG_AUTO aperture is scaled to 5.0 times the Kron radius of the galaxy. MAG_AUTO is only used to determine z_{850} magnitudes; $i_{775} - z_{850}$ colors are determined using PSF matching and a smaller aperture, as described in Meyers10.

5.2. *Galaxy Detection Completeness and Magnitude Bias*

To count all the flux in all cluster galaxies, we must make two corrections: (1) add the galaxy light outside of the MAG_AUTO aperture, and (2) add the luminosity of all cluster galaxies below the detection threshold of our galaxy catalog. We use a Monte Carlo simulation of galaxies placed on our real survey data to determine both the detection efficiency as a function of galaxy magnitude, and the fraction of galaxy light inside the MAG_AUTO aperture. Each simulated galaxy has a Sérsic (1968) profile, with the Sérsic index n simply selected from a flat distribution ranging from $n = 0.7$ to $n = 4.5$, and the minor to major axis ratio q selected from a flat distribution ranging from $q = 0.3$ to $q = 1$. The distribution of galaxy angular sizes will also affect the results.
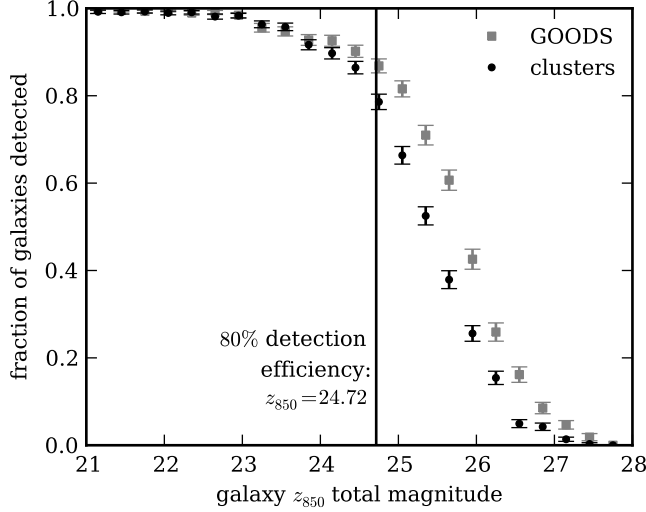
Figure 8. Percentage of simulated galaxies recovered by SEXTRACTOR as a function of total galaxy z_{850} magnitude for simulated galaxies placed on cluster fields (*black circles*) and GOODS fields (*grey squares*). The detection efficiency drops to 80% at $z_{850} = 24.72$ for cluster fields (*vertical line*). We discard all galaxies dimmer than this value.
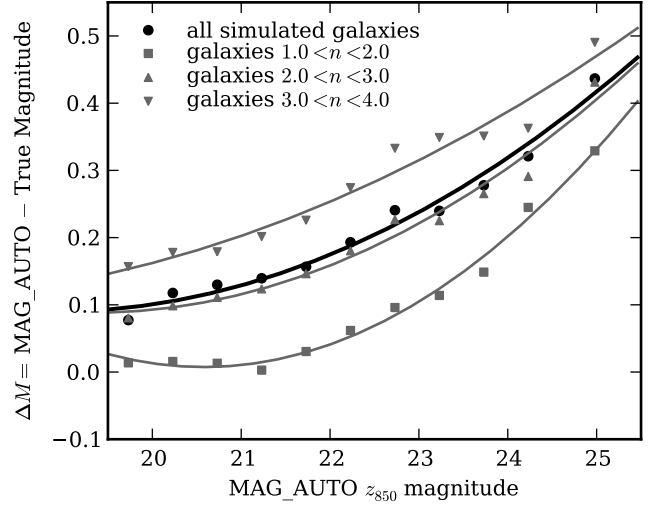

Figure 9. Galaxy MAG_AUTO aperture correction as a function of galaxy magnitude. *Black circles:* Average correction for the full distribution of galaxies simulated, including all Sérsic indices n. The *black line* is a fit to these points and is the relation we use. Note that it is not extrapolated beyond the range shown. To illustrate the effect of n on the aperture correction, we plot the aperture correction for subsets of galaxies with different Sérsic indices (*Grey squares and triangles*). Galaxies with larger Sérsic indices have a larger aperture correction.

For guidance on the size of the galaxies of concern (namely, those at $z \gtrsim 0.9$) we turned to the subsample of the 672 galaxies having spectroscopic redshifts $0.85 < z < 1.6$. These 672 galaxies were all fit with GALFIT (Peng et al. 2002), which fits a value for r_e. Based on the distribution of r_e as a function of magnitude for these galaxies, we chose r_e for each simulated galaxy (based on its magnitude). A total of 15000 and 12000 simulated galaxies were placed on cluster and GOODS fields respectively.

The detection efficiency as a function of galaxy magnitude is shown in Figure 8. For the average of all cluster fields, the detection efficiency drops to 80% at $z_{850} = 24.72$. We use this magnitude as a cutoff in our selection, discarding all galaxies dimmer than this magnitude. We later correct total cluster luminosities for the uncounted light from these galaxies by using an assumed cluster luminosity function. In reality, the detection efficiency varies slightly from field to field (and even within a field) due to exposure time variations. However, to first order, the variation is accounted for by using the average efficiency in all fields. In addition, the total luminosity of $z_{850} > 24.72$ cluster galaxies is expected to be small (as we show below), so slight changes in the cutoff will have a negligible effect on the total luminosity.

For each simulated galaxy, we determine the difference (ΔM) between the MAG_AUTO magnitude and the true total magnitude. Binning the simulated galaxies by their MAG_AUTO magnitude, we derive a relation between ΔM and the galaxy brightness (Fig. 9, black circles). ΔM generally increases with galaxy magnitude because the outskirts of dimmer galaxies are increasingly buried in noise, causing SEXTRACTOR to underestimate the true extent of the galaxy, and thereby underestimate the Kron radius, resulting in a smaller MAG_AUTO aperture. We find that the relation is well-fit by a second-order polynomial (Fig. 9, thick black line), given by

$$\Delta M = 0.238 + 0.081(M_{MAG\_AUTO} - 23) + $$
$$+ 0.009(M_{MAG\_AUTO} - 23)^2. \qquad (7)$$

We use this to correct the magnitude of each detected galaxy.

Note that the correction is not extrapolated beyond the fitted range shown.

Because we cannot reliably determine r_e or the Sérsic index n for each galaxy, we rely on the simulated distribution of r_e and n to accurately represent the true distributions. (The black circles in Fig. 9 include all simulated galaxies.) We have based our distribution of r_e on actual galaxies, but n is less well-known. To estimate the effect of varying the n distribution, we show ΔM for subsets of the simulated galaxies, divided by Sérsic index (Fig. 9, grey points and lines). ΔM increases with Sérsic index, because a larger Sérsic index implies a larger fraction of light in the outskirts of the galaxy, under the detection threshold. This leads to a smaller estimate of the Kron radius, and a smaller MAG_AUTO aperture. If, instead of the flat $1 < n < 4$ distribution used, all galaxies had $1 < n < 2$, the aperture correction would be lower by approximately 0.10 magnitudes. If instead all galaxies had $3 < n < 4$, the correction would be higher by approximately 0.07 magnitudes. We use 0.07 mag as the systematic uncertainty in the aperture correction. (All systematic uncertainties are summarized in §6.2 and Table 8.)

5.3. K-Corrections

We use a K-correction based on the BC03 stellar population spectral models to convert the observed z_{850} magnitude to a rest-frame B magnitude for each cluster. Rather than using a single K-correction for all the light in each cluster, we apply a K-correction to each galaxy magnitude based on its $i_{775} - z_{850}$ color. For each cluster's redshift, we determine the relation between K-correction (M_B (rest) $-z_{850}$) and $i_{775} - z_{850}$ color, using BC03 spectra with initial metallicities in the range $0.004 < Z < 0.05$ and ages in the range $1 \times 10^8 - 5 \times 10^9$ yr. For most cluster redshifts in our sample, all of the spectra over this wide range fall along the same line in K-correction versus color, meaning that the color determines the K-correction, regardless of the metallicity or age assumed. The dispersion of the models about the best-fit line

is < 0.03 mag at redshifts $\lesssim 1.1$ and $\gtrsim 1.4$, and reaches its largest value of 0.09 mag at $z = 1.26$. We calculate the K-correction for each galaxy using this best-fit relation, effectively assuming that every galaxy is at the cluster redshift. This results in an incorrect luminosity for non-cluster member galaxies, but this is accounted for by performing the same K-correction on the galaxies in the GOODS fields prior to subtracting their luminosity.

5.4. *Luminosity function correction*

We estimate the total luminosity of all galaxies below the detection limit of $z_{850} = 24.72$ using a Schechter (1976) luminosity function, which gives the number of galaxies in the luminosity interval $[L, L + dL]$ in a given sample,

$$\Phi(L)dL = \Phi^*(L/L^*)^\alpha e^{-L/L^*} d(L/L^*). \qquad (8)$$

Φ^* is a normalization, L^* is a characteristic galaxy luminosity, and α is a unit-less constant. The ratio of total to observed luminosity is then

$$C = \frac{\int_0^\infty L\Phi(L)dL}{\int_{L_{lim}}^\infty L\Phi(L)dL}, \qquad (9)$$

and we multiply each observed cluster luminosity by C to get the total luminosity.

We assume values for L^* and α determined in other studies and use our data to perform a rough consistency check. For α, studies have shown that the value does not evolve much from low redshift, at least for redder galaxies. Analyzing only red galaxies in 28 clusters spanning $0 < z < 1.3$, Andreon (2008) find $\alpha = -0.91 \pm 0.06$ (rest-frame V-band) with no discernible trend in redshift (see also Andreon 2006b,c). From five intermediate-redshift clusters ($0.54 < z < 0.9$), Crawford et al. (2009) find a somewhat flatter faint-end slope $\alpha \sim -0.6$ (rest-frame B-band) for the red-sequence luminosity function. Looking at the full luminosity function, Goto et al. (2005) find $\alpha = -0.82 \pm 0.10$ in one cluster at $z = 0.83$ (rest-frame B-band), compared to $\alpha = -1.00 \pm 0.06$ in 204 low-redshift clusters (rest-frame g-band) (Goto et al. 2002). In redder bands, Strazzullo et al. (2006) find $\alpha \sim -1$ for three clusters at redshifts $1.11 < z < 1.27$ (in approximately rest-frame z band). Summarizing, most studies find a value consistent with $\alpha \sim -0.9$, and we assume this value in computing C.

Values for M^* are also reported in most of the above-mentioned studies. Studies of red galaxies find that the variation of M^* with redshift is consistent with passive evolution, with M^* decreasing towards higher redshifts (Andreon 2006c; Crawford et al. 2009). Crawford et al. (2009) find $M_B^* = -21.1$ and $M_B^* \sim -21.3$ (with errors of approximately a half magnitude) for two clusters at redshifts 0.75 and 0.83. K-correcting from the observed [3.6]-band, Andreon (2006c) find $M_B^* \sim -21.7$ at $z \sim 1.1$, with approximately 0.5 magnitudes of evolution between $z = 0.3$ and $z = 1.1$. At lower redshift (considering all galaxies) Goto et al. (2002) find $M_B^* \sim -21.6$, compared to $M_B^* \sim -21.0$ for one cluster at $z = 0.83$ (Goto et al. 2005). On the basis of these measurements, we assume a value of $M_B^* = -21.7$.

We have checked our assumed M_B^* and α for consistency with our data. With the set of spectroscopically-confirmed cluster galaxies from our clusters at $z < 1.2$, we confirmed that the bright end of the luminosity function is consistent with $M_B^* = -21.7$, and strongly inconsistent with values out-

Table 5
Bright cutoff magnitudes and luminosity function parameters

ID	z	Cutoff from	$M^{\mathrm{bright}}_{z_{850},\mathrm{obs}}$	$M^*_{z_{850},\mathrm{obs}}$	C
A	1.45	Max cD	21.06	22.80	1.143
B	1.12	cD	20.11	21.38	1.033
C	0.98	cD	19.87	20.79	1.018
D	1.02	BCG	20.13	20.95	1.021
E	1.03	cD	19.40	20.99	1.022
F	1.11	Max cD	19.63	21.34	1.031
G	1.26	BCG	20.34	22.04	1.064
H	1.24	BCG	20.33	21.95	1.058
I	1.34	Max cD	20.65	22.37	1.092
J	1.37	Max cD	20.77	22.50	1.104
K	1.41	Max cD	20.92	22.65	1.122
L	1.37	Max cD	20.77	22.50	1.104
M	0.92	Max cD	18.78	20.53	1.014
N	1.03	BCG	20.22	20.99	1.022
P	1.1	Max cD	19.58	21.29	1.030
Q	0.95	cD	20.01	20.66	1.015
R	1.22	Max cD	20.15	21.86	1.054
S	1.07	Max cD	19.44	21.16	1.026
T	0.97	Max cD	19.00	20.75	1.017
U	1.04	Max cD	19.31	21.04	1.022
V	0.91	cD	18.89	20.49	1.013
W	1.26	Max cD	20.33	22.04	1.064
X	1.11	Max cD	19.63	21.34	1.031
Y	1.23	cD	20.29	21.90	1.056
Z	1.39	cD	20.85	22.58	1.112

Note. — "Cutoff from" refers to how M^{bright} is determined. "cD": magnitude of visually central dominant galaxy. "BCG": magnitude of visually classified brightest cluster elliptical (but not central) galaxy. "Max cD": Cluster does not have obvious cD galaxy or clear BCG. In this case, M^{bright} is K-corrected from $M_B = -23.42$, the absolute magnitude of the brightest cD galaxy in the entire sample.

side the range $M_B^* = -21.7 \pm 0.5$. We also determined the luminosity function using a statistical subtraction of the "background" luminosity function from the GOODS fields, finding excellent agreement with the assumed M_B^* and α values over the range $-24 < M_B < -19.8$ ($M_B = -19.8$ corresponds to the detection limit in the highest-redshift clusters).

For each cluster, we calculate C in the observer frame, converting $M_B^* = -21.7$ to the observed z_{850} band, using the cluster redshift and a K-correction based on a passive galaxy template. In Table 5 we report the value $M^*_{z_{850},\mathrm{obs}}$ and the resulting correction C for each cluster. The correction is less than 5% for the majority of clusters, rising to a maximum of 14% for the highest-redshift cluster. Varying M_B^* by ± 0.5 mag changes the average correction by only $^{+4}_{-2}\%$, which we take as the systematic uncertainty in the faint-end luminosity correction (§6.2).

5.5. *Cluster Luminosities and Aggregate Cluster Profile*

For each cluster we sum the K-corrected B-band luminosity of all galaxies brighter than the detection limit $z_{850} = 24.72$ and dimmer than the bright cutoff magnitude, $M^{\mathrm{bright}}_{z_{850},\mathrm{obs}}$, listed in Table 5. In clusters with a central dominant (cD) galaxy or dominant (but not central) brightest cluster galaxy(BCG), the bright cutoff magnitude is set to the magnitude of the cD galaxy or BCG. In clusters lacking a clearly dominant galaxy, we conservatively set the cutoff based on the absolute magnitude of the most luminous cD galaxy in any cluster, $M_B = -23.42$ (from cluster XMMU J2235.3−2557).

For each cluster we apply the same selection criteria and K-corrections to the GOODS fields to determine the "background" specific to that cluster. The error in the luminos-

ity comes from the error in this background determination, which we estimate in the following way: We select 30 non-connected circular regions (15 in each of GOODS North and South) of radius $1.4'$, similar to the size of the cluster fields. We determine the luminosity density in each of these fields. The average is taken as the background luminosity for the cluster, and the standard deviation (typically $15-20$ % of the average) is taken as the error in this "background" luminosity due to variations between fields.

We have implicitly assumed that the GOODS average accurately represents the cosmic average. GOODS incorporates only two widely separated fields. As a result, the average luminosity density may differ from the cosmic average due to variations in large scale structure. As a rough estimate of the cosmic variance, we compare the two GOODS fields. The average luminosity density of the GOODS-North regions is consistently higher than that of the GOODS-South regions by $15-20\%$. This means that the "standard deviation" of these two samples of large scale structure is $\sim 8\%$. We checked this using the cosmic variance calculator made available by Trenti & Stiavelli (2008)[30]. The expected cosmic variance in galaxy number counts in the redshift window $0.7 < z < 1.7$ for one GOODS field is approximately $\sim 6\%$, in good agreement with our naïve estimate. Conservatively, we take 8% as the cosmic variance for one GOODS field. For the *average* of the North and South fields, this implies a cosmic variance of $8\%/\sqrt{2} \sim 6\%$.

One might be additionally concerned that the "background" in the cluster fields is biased higher than the cosmic average because clusters form in regions of large-scale overdensities. However, each cluster field is a "pencil-beam" galaxy survey, so the vast majority of non-cluster galaxies will not be associated with the high-density region in which each cluster formed.

Ideally one would measure a two-dimensional luminosity density, $L(x,y)$, for each cluster, as in Equation (2). However, the large background makes this difficult. For our purpose (which is to account for variations in control time with radius), it is sufficient to assume the clusters have a circularly symmetric luminosity distribution, $L(r)$. For each cluster, we sum the total luminosity in annuli of width 0.1 Mpc. For nearly all clusters there is a clear overdensity relative to the background out to $r \sim 0.3$ Mpc. Beyond 0.3 Mpc, the luminosity measurement is dominated by background noise for most clusters. This might appear to be a problem; we wish to characterize the cluster luminosities out to $r \gtrsim 0.7$ Mpc, the area over which we searched for SNe. In fact, it is only necessary to accurately measure the *average* luminosity profile over the full area (the denominator of Eq. 1 is the sum of the cluster luminosities, weighted by control time). Averaging all 25 clusters, there is a significant measurement of the luminosity profile out to > 0.5 Mpc (Fig. 10, left panels), and the average cluster luminosity within $r < 0.6$ Mpc has an error of 12% (statistical only) and $\sim 20\%$ (statistical + cosmic variance), below the Poisson error in the number of SNe detected.

Beyond $r < 0.6$ Mpc, the control time is generally small (that is, there are few observations covering the outskirts of the clusters) and the cluster luminosity density is low, meaning that these regions will not contribute greatly to the rate measurement. Still, we include these regions in our rate cal-

culation, using the entirely reasonable prior that the luminosity density is decreasing with radius past $r < 0.6$ Mpc. How rapidly the luminosity density decreases will not have a significant impact on the result, but as a convenient analytic description we fit a β-model of the form

$$L(r) = \frac{\Sigma_0}{(1 + (r/r_{\mathrm{core}})^2)^\beta} \qquad (10)$$

over the range $r < 0.6$ Mpc and apply this function at $r > 0.6$ Mpc. The data are well-fit by this model, with best-fit parameters $r_{\mathrm{core}} = 0.074$ Mpc and $\beta = 0.91$. Varying this model luminosity by $\Delta\Sigma_0 = \pm20\%$ (easily enclosing the allowed range of $L(r)$) only changes our results by $\pm4\%$. This and other systematic uncertainties are summarized in Table 8.

5.6. *Galaxy subsets*

In addition to measuring the total luminosity of all galaxies in the clusters, we also measure the total luminosity of only red-sequence galaxies and the total luminosity of only red-sequence, morphologically early-type galaxies. These measurements enable us to compute the cluster SN Ia rate specifically in these galaxy subsets. For the red-sequence-only measurement we follow the same procedure as above, but eliminate from the analysis all galaxies with $i_{775} - z_{850}$ colors more than 0.2 mag from their respective cluster red sequences (galaxy colors and cluster red sequences are determined as in Meyers10). For the red-sequence early-type measurement, we make the same requirement in color, and additionally use the quantitative morphology requirements of Meyers10. Meyers10 use two parameters, asymmetry and Gini coefficient, to automatically divide galaxies into early- and late-type subsets. Here we require the asymmetry to be < 0.10 and the Gini coefficient to be > 0.40. We also require the galaxies to be $z_{850} < 24$ as the asymmetry and Gini coefficient are somewhat less reliable at fainter magnitudes.

The luminosity profiles for these two subsets are shown in the center and right columns of Figure 10. The profiles are broadly consistent with the profile of the full cluster luminosity (left column), but the "subset" profiles are much better measured. This is because by excluding bluer galaxies, we have eliminated much of the background while still retaining the majority of cluster galaxies. The red-sequence subset contains 77% of the luminosity of the full cluster within 0.6 Mpc (Table 6). The red-sequence early-type subset has 62% of the light contained in the red-sequence subset. However, keep in mind that in the early-type subset we have excluded $z_{850} > 24$ galaxies, whereas they are included in the red-sequence subset: In fact 68% of $z_{850} > 24$ red-sequence galaxies pass the "early-type" morphology requirements.

Note that our definition of "red-sequence" here is a relatively simple one. It is sufficient to select a subsample of "more red" galaxies for the purpose of looking for a dependence of the SN rate with galaxy color within the cluster. However, for measuring the red fraction in clusters (e.g., the Butcher-Oemler effect (Butcher & Oemler 1978, 1984)), defining red-sequences with a constant color width for all redshifts is not ideal (Andreon 2006a). The luminosity content of the subsets are reported above only to give the relative size of each sample; a full analysis of the cluster content is beyond the scope of this paper.
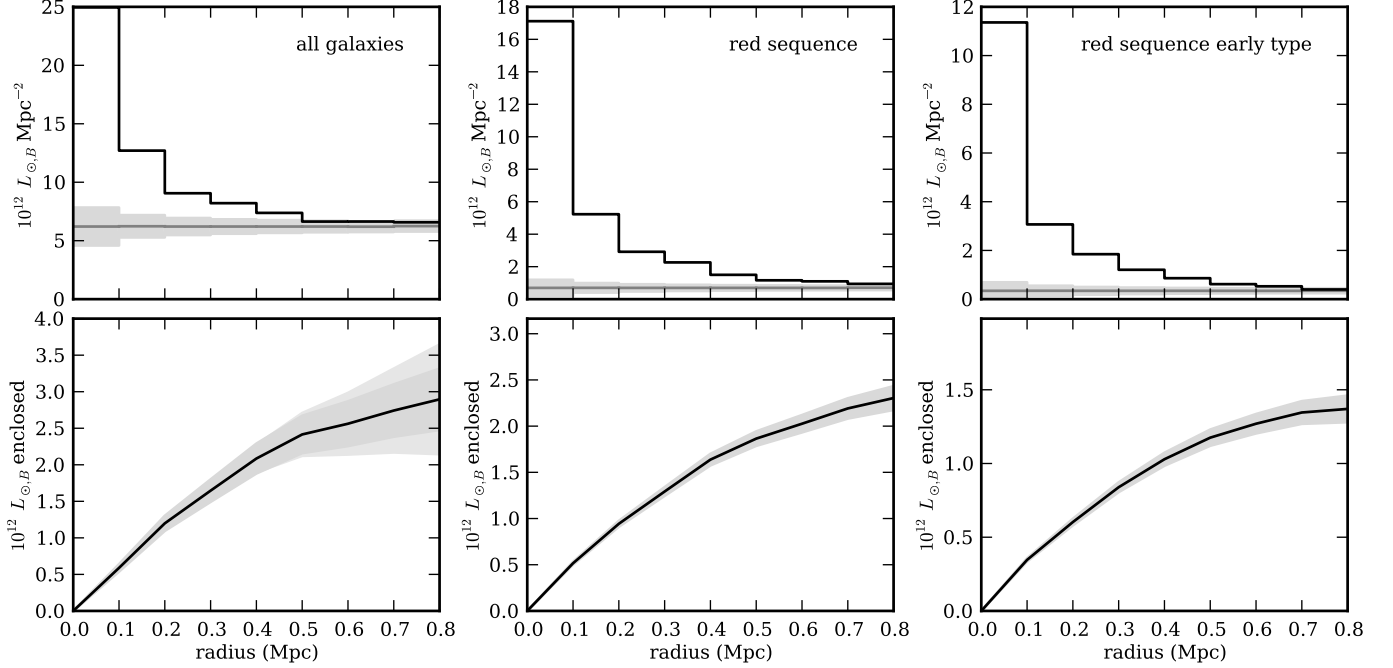
---

[30] http://casa.colorado.edu/~trenti/CosmicVariance.html

Figure 10. Average luminosity profile of the 25 clusters. *Top row:* Average luminosity density in the cluster fields in annuli of width 0.1 Mpc extending out from the cluster center. The grey line and shaded region show the estimated "background" luminosity in each annulus and the error on that background, respectively. The darker grey region is the statistical-only error, while the light grey is the statistical + cosmic variance error, added in quadrature. *Bottom row:* The total enclosed luminosity as a function of radius, derived by subtracting the background from the total luminosity density in each bin in the top row plot. The left plots include galaxies of all colors and morphologies, while the center plots include only galaxies with $i_{775} - z_{850}$ colors within ± 0.2 mag of the red sequence in their respective clusters. The right plots include only galaxies that satisfy the color requirement and also have $z_{850} < 24$ and are morphologically early type. By excluding bluer galaxies (center and right plots) the background (and error) is reduced dramatically.

Table 6
Average cluster luminosities within $r < 0.6$ Mpc

Cluster subset	N_{clusters}	$\bar{z}$	All galaxies ($10^{12}L_{\odot,B}$)	RS galaxies ($10^{12}L_{\odot,B}$)	RSE galaxies ($10^{12}L_{\odot,B}$)
X-ray discovered	9	1.20	$2.85 \pm 0.54 \pm 0.44$	$2.41 \pm 0.16 \pm 0.05$	$1.47 \pm 0.12 \pm 0.02$
IR-Spitzer discovered	7	1.30	$2.88 \pm 0.70 \pm 0.52$	$1.83 \pm 0.24 \pm 0.07$	$0.96 \pm 0.16 \pm 0.03$
Optical discovered	9	1.00	$2.02 \pm 0.37 \pm 0.32$	$1.79 \pm 0.09 \pm 0.03$	$1.31 \pm 0.06 \pm 0.01$
$z < 1.2$	14	1.03	$2.18 \pm 0.31 \pm 0.33$	$1.82 \pm 0.07 \pm 0.03$	$1.31 \pm 0.05 \pm 0.01$
$z > 1.2$	11	1.32	$3.04 \pm 0.57 \pm 0.54$	$2.28 \pm 0.19 \pm 0.07$	$1.22 \pm 0.14 \pm 0.04$
All Clusters	25	1.16	$2.56 \pm 0.31 \pm 0.42$	$2.02 \pm 0.09 \pm 0.05$	$1.27 \pm 0.07 \pm 0.02$

Note. — "RS": galaxies within ± 0.2 mag of the cluster red sequence. "RSE": galaxies fulfilling the "RS" requirement, and also $z_{850} < 24$, and morphologically early-type. The first and second confidence intervals are the statistical error and cosmic variance error, respectively. These luminosities do not include the faint-galaxy correction C.

5.7. *Stellar Mass-to-Light Ratio*

In order to compare SN rates at different redshifts or in different environments, rates must be normalized by stellar mass rather than stellar luminosity. Here, we convert our luminosity measurements to stellar mass measurements using an assumed stellar mass-to-light ratio. The observed z_{850} band corresponds to approximately rest-frame B-band for the most of the clusters. In general, B-band light is not a good tracer of stellar mass, as it is sensitive to small amounts of young stars (see, e.g. Mannucci et al. 2005). However, the majority of the cluster light comes from red-sequence galaxies with little or no recent star formation. For these galaxies, B-band light is not heavily affected by young stars and provides a reasonable stellar mass estimate. To account for a reduced mass-to-light ratio in the bluer galaxies, we use an assumed color-dependent mass-to-light ratio and the observed $i_{775} - z_{850}$ galaxy color to obtain a mass-to-light ratio on a galaxy-by-galaxy basis.

Bell et al. (2003, hereafter Bell03) derive color-dependent mass-to-light ratios as a function of various rest-frame galaxy colors. These mass-to-light ratios have been used in the lower-redshift cluster rate studies of Sharon et al. (2007), Sharon et al. (2010), and by extension, Dilday et al. (2010). We chose to use the same mass-to-light ratio for consistency. However, the Bell03 relations are based on $ugrizK$ photometry of low-redshift galaxies, corrected for evolution to $z = 0$. As such, they are not directly applicable at high redshift. A stellar population passively evolving from age $\sim$ a few Gyr (at $z \sim 1$) to > 10 Gyr (at $z = 0$) will dim significantly while only growing slightly redder (see, e.g. BC03), in a manner that does not follow the Bell03 relations.

Bell03 derived stellar masses by fitting a grid of PÉGASE2 (Fioc & Rocca-Volmerange 1997) synthetic galaxy spectral energy distributions (SEDs) to galaxy photometry. They assumed a galaxy formation redshift of $z_f = 4$ and an
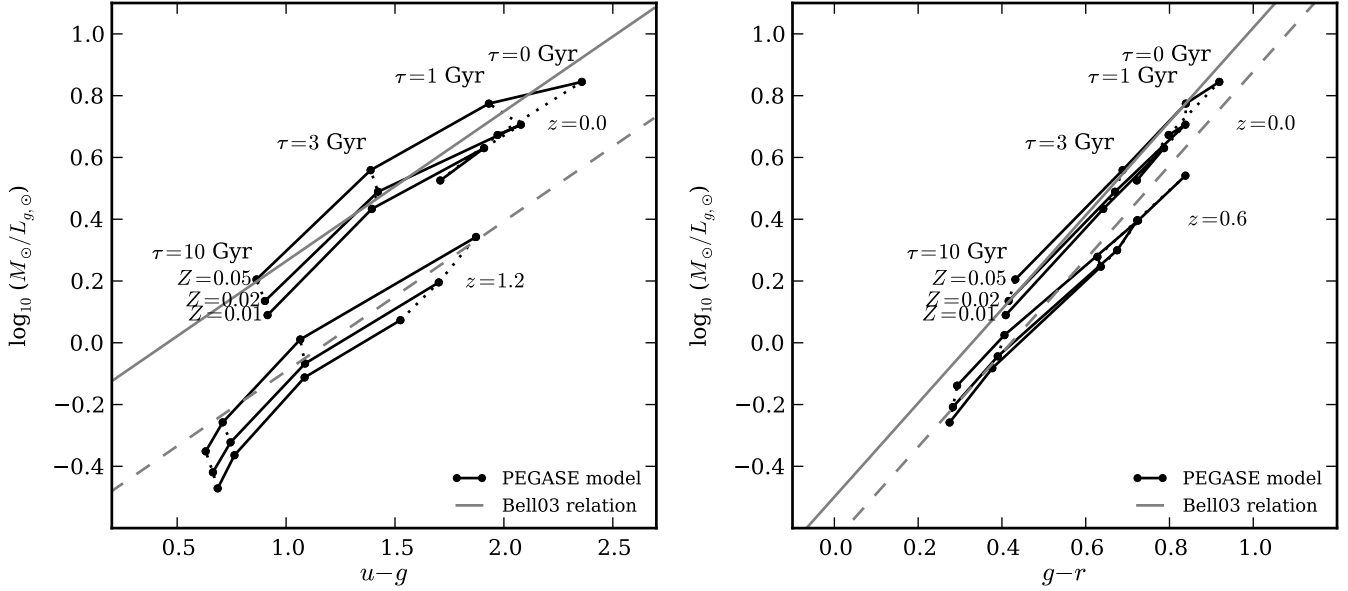
Figure 11. Evolution of mass-to-light ratio versus color with redshift. *Left panel:* Mass-to-light ratio as a function of $u - g$ color at $z = 0$ and at $z = 1.2$ (typical redshift in this study). The grid of points show PÉGASE2 models with exponentially-decreasing star formation rates, with various time constants τ and metallicities Z. A formation redshift of $z_f = 4$ is assumed. As the models are evolved back in time from an observed redshift of $z = 0$ to an observed redshift of $z = 1.2$, the mass-to-light ratio decreases and moves away from the Bell03 relation (*solid grey line*). The *dotted grey line* shows the relation used in this study for $z = 1.2$. At $z = 1.2$ the offset from the Bell03 relation is -0.36 dex, or a factor of 0.43. *Right panel:* Same as left panel, but for $g - r$ color and for an observed redshift of $z = 0.6$, the typical redshift in the rate study of Sharon et al. (2010). The offset here is only -0.14 dex, or a factor of 0.72.

exponentially-decreasing or -increasing star formation history. To estimate the effect of evolution from their $z = 0$ relation to higher-redshift, we make a similar grid of PÉGASE2-generated SEDs and evolve them backwards in time from $z = 0$ (Fig. 11). For $u - g$ color, Bell03 derive a mass-to-light ratio of $\log_{10}(M_\odot/L_{g,\odot}) = -0.221 + 0.485(u - g)$ at $z = 0$. We find that at higher redshifts, the models are well-fit by a relation with the same slope, but smaller normalization. The best-fit offset from the $z = 0$ relation is -0.26 dex at $z = 0.9$ and -0.44 dex at $z = 1.45$. We therefore assume a mass-to-light ratio of

$$\log_{10}(M_\odot/L_{g,\odot}) = \begin{cases} -0.48 + 0.485(u - g), & z = 0.9 \\ -0.66 + 0.485(u - g), & z = 1.45 \end{cases}$$ (11)

and linearly interpolate for intermediate redshifts ($z = 1.2$ is shown in Fig. 11). We have cross-checked these evolution offsets using the stellar population templates of BC03 (with the standard Padova 1994 evolution) and find results consistent within 0.03 dex.

For each galaxy, we K-correct the observed i_{775} and z_{850} magnitudes to rest-frame SDSS u and g magnitudes using the method discussed in §5.3, and convert to a stellar mass using the above mass-to-light ratios. The cumulative mass-to-light ratio (the ratio of the total mass of all 25 clusters to the total luminosity of all 25 clusters) is $M_\odot/L_{g,\odot} = 1.25$ (see Table 7, "denom"). For red-sequence galaxies only, the ratio is higher ($M_\odot/L_{g,\odot} = 1.38$) due to the exclusion of bluer galaxies with a lower inferred mass-to-light ratio.

6. RESULTS AND SYSTEMATIC UNCERTAINTIES

Here we present our results for the full cluster rate and for two galaxy subsets (§6.1) and summarize contributions to the uncertainty (§6.2) in each. In §6.3 we show that the rate result in the subsets are not sensitive to the specific parameters used to select the subset.

6.1. *Results*

The results are presented in Table 7. We derive a rate in the full cluster, in red-sequence galaxies only, and in red-sequence early-type galaxies only. Each subset includes a different number of SNe: As discussed in §3.4, we have discovered 8 ± 1 cluster SNe, where the quoted uncertainty is due to classification uncertainty (including uncertainty in both SN type and cluster membership). Limiting the sample to only SNe discovered in galaxies included in the red-sequence subset excludes SN SCP06F12 and SN SCP06C1 are eliminated, leaving 6.5 ± 0.5 cluster SNe Ia. The uncertainty here comes from the uncertainty in the cluster membership and type of SN SCP06E12, which we count 0.5 ± 0.5 cluster SNe Ia. Further limiting the sample to only SNe discovered in galaxies included in the red-sequence early-type subset, SN SCP06E12 is eliminated as its host galaxy is dimmer than the $z_{850} = 24$ cutoff used for this subset leaving 6 SNe Ia with negligible classification error. The number of SNe Ia discovered in each subset, including classification error, is summarized in Table 7 under $N_{\rm SN\ Ia}$.

We normalize the rate in three different ways: by B-band luminosity, by g-band luminosity, and by stellar mass. For each cluster, we use the visibility time map $T(x,y)$ (e.g., Fig. 7) and the measured luminosity (or mass) profile to carry out the integral in equation (2) giving the time-luminosity searched. The sum of these values for all 25 clusters is the denominator of equation (1), the total time-luminosity searched in all clusters. This is shown in Table 7 under "Denom" for each sample. The rate is simply $N_{\rm SN\ Ia}$ divided by "denom," as in equation (1). The contributions to the statistical and systematic errors are summarized in Table 8.

The weighted-average redshift, $\bar{z}$, for each subsample is given by

$$\bar{z} = \frac{\sum_i z_i \int_{x,y} T_i(x,y) L_i(x,y)}{\sum_i \int_{x,y} T_i(x,y) L_i(x,y)},$$ (12)

Table 7
Results

Environment	Unit	$\bar{z}$	$N_{\text{SN Ia}}$	Denom	Rate	(stat)	(sys)
Full cluster	SNuB	1.14	8.0 ± 1.0	15.87	0.50	$+0.23$ -0.19	$+0.10$ -0.09
Full cluster	SNug	$\cdots$	$\cdots$	15.96	0.50	$+0.23$ -0.19	$+0.10$ -0.08
Full cluster	SNuM	$\cdots$	$\cdots$	22.41	0.36	$+0.16$ -0.13	$+0.07$ -0.06
Red-sequence	SNuB	1.13	6.5 ± 0.5	11.95	0.54	$+0.25$ -0.19	$+0.07$ -0.07
Red-sequence	SNug	$\cdots$	$\cdots$	12.20	0.53	$+0.24$ -0.19	$+0.07$ -0.07
Red-sequence	SNuM	$\cdots$	$\cdots$	17.61	0.37	$+0.17$ -0.13	$+0.05$ -0.05
Red-sequence early-type	SNuB	1.10	6.0 ± 0.0	7.29	0.82	$+0.39$ -0.30	$+0.09$ -0.08
Red-sequence early-type	SNug	$\cdots$	$\cdots$	7.59	0.79	$+0.38$ -0.29	$+0.09$ -0.08
Red-sequence early-type	SNuM	$\cdots$	$\cdots$	11.77	0.51	$+0.24$ -0.19	$+0.06$ -0.05

Note. — "Denom" is the denominator of equation (1) and has units of $10^{12} L_{\odot,B}$ years, $10^{12} L_{\odot,g}$ years and $10^{12} M_{\odot}$ years for rate units of SNuB, SNug and SNuM respectively.

Table 8
Sources of Uncertainty

Source of error	Full cluster (%)	Red-sequence (%)	Red-sequence early-type (%)
Statistical			
Poisson	$+40$ -32	$+45$ -35	$+47$ -36
Luminosity (stat)	± 12	± 6	± 6
Luminosity (cosmic var.)	± 16	± 4	± 3
Total statistical	$+45$ -38	$+46$ -35	$+48$ -37
Systematic			
SN type classification	± 13	± 8	$\cdots$
Control time: varying M_B	$+8$ -6	$+8$ -6	$+8$ -6
Control time: dust distribution	$+10$ -2	$\cdots$	$\cdots$
Luminosity: MAG_AUTO corr.	± 7	± 7	± 7
Luminosity: K-correction	± 3	± 3	± 3
Luminosity: Faint galaxy corr.	$+2$ -4	$\cdots$	$\cdots$
Luminosity: $r > 0.6(0.8)$ Mpc	± 4	± 1	± 1
Total systematic	$+20$ -17	$+14$ -12	$+11$ -10
Total statistical + systematic	$+49$ -42	$+48$ -37	$+49$ -38

where z_i, L_i and T_i are the redshift, luminosity and effective visibility time of the i-th cluster, respectively. The weighted-average redshift is slightly smaller for the red-sequence and red-sequence early-type galaxy subsets. This is because in the higher-redshift clusters, a smaller fraction of galaxies meet the subset requirements (see $z < 1.2$ versus $z > 1.2$ average cluster luminosity in Table 6).

6.2. *Summary of Systematic Uncertainties*

Throughout the paper, we have highlighted and addressed possible sources of systematic uncertainty. Here we summarize these sources. In Table 8 we show the relative contribution of each to the total systematic error, and compare to sources of statistical error.

(1) *SN type classification:* The uncertainty in the number of SNe observed in each galaxy subset was addressed in §6.1. The fractional error in the rate is simply the fractional error in the number observed.

(2) *Control time: Varying M_B:* In our control time simulations, we assumed a distribution of SN Ia light curve shapes and absolute magnitudes. To first order, the impact of these

assumptions on the control time is captured by varying the assumed SN Ia absolute magnitude (§4.3). Variations of ± 0.2 mag resulted in a rate change of $^{+8}_{-6}\%$

(3) *Control time: dust distribution:* In §4.3 we assessed the impact of varying amounts of dust extinction on the control time. Assuming an unrealistically large amount of dust-affected SNe decreased the control time by 9% (increasing the SN rate by 10%), while decreasing the amount of dust-affected SNe increased the control time by 2% (decreasing the SN rate by 2%). We do not apply this systematic error to the red-sequence or red-sequence early-type subsets, as we have independent evidence that the amount of dust is limited in these environments.

(4) *MAG_AUTO correction:* In computing the total z_{850} luminosity of each galaxy, we made a correction to the MAG_AUTO magnitude ranging from $\sim 10\%$ at $z_{850} = 20$ to $\sim 30\%$ at $z_{850} = 25$. Varying the range of n used in the simulation by ± 1 affects the correction by $\pm 7\%$.

(5) *K-correction:* In §5.3, we noted that the scatter of BC03 templates about the best-fit K-correction is typically less than 0.03 mag. We use this value as the systematic error on the K-correction.

(6) *Faint galaxy correction:* The average correction C reported in Table 5 is 1.054. Varying M^* by ± 0.5 magnitudes results in an average correction of 1.032 and 1.092 for -0.5 and $+0.5$ magnitudes, respectively. Thus, we assign $^{+2\%}_{-4\%}$ as the systematic error on the rate associated with this correction. This error is not applied to the red-sequence or red-sequence early type subsets as faint galaxy light is counted in these subsets.

(7) *Luminosity at large radii:* In §5.5 we assumed a model for the cluster luminosity profile at $r > 0.6$ Mpc (0.8 Mpc for red-sequence and red-sequence early-type subsets). Varying the model luminosity by $\pm 20\%$ resulted in a $\pm 4\%$ change in the full cluster rate. The change is much smaller ($\pm 1\%$) for the red galaxy subsets because the model is only used at $r > 0.8$ Mpc.

6.3. *Effect of Varying Subset Requirements*

In selecting our red-sequence and red-sequence early-type galaxy subsamples, we required red-sequence galaxies to be within ± 0.2 mag of the color of their cluster red sequence. For early-type galaxies, we required the asymmetry parameter to be < 0.1 and the Gini coefficient to be > 0.40. It is interesting to test the sensitivity of the results to variations in
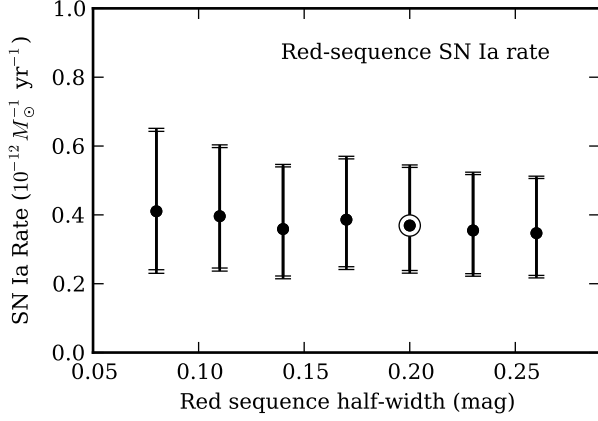
Figure 12. The effect of varying the width of the red sequence. The nominal red-sequence rate result corresponds to a half-width of 0.20 mag. The inner and outer error bars represent the statistical and total uncertainty, respectively.
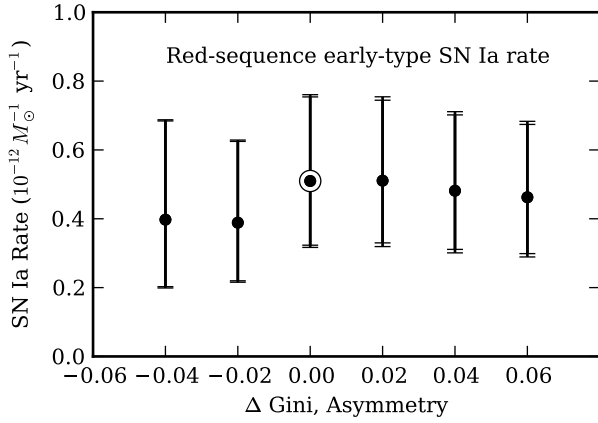

Figure 13. The effect of varying the morphology parameter requirements. Negative Δ values correspond to a more strict selection and a higher-purity early-type galaxy sample. The requirements are asymmetry $< 0.1 + \Delta$ and Gini coefficient $> 0.40 - \Delta$. The nominal red-sequence early-type rate corresponds to $\Delta = 0$. The red-sequence half-width is fixed at 0.2 mag. The inner and outer error bars represent the statistical and total uncertainty, respectively.

the requirements. In Figures 12 and 13 we vary the requirements and observe the effect on the rates. As requirements are made more strict (for example, narrowing the red sequence) the total mass of the sample decreases. At the same time, SNe fall out of the sample when their host galaxies are cut. The Poisson error increases as the number of included SNe shrinks.

There is not a strong dependence of the SN Ia rate with galaxy color residual from the red sequence (Fig. 12). Even in cluster galaxies that lie in a tight range around the red-sequence (±0.08 mag), we find a SN Ia rate consistent with the full cluster rate. Similarly, there is no significant rate trend with the purity of the early-type sample (Fig. 13). We happened to pick morphology requirements that yield a slightly higher rate than other choices, but such variations are expected with small-number statistics and are accounted for by the Poisson uncertainty in the result (Tables 7 and 8). Even in the most-selective subset ($\Delta = -0.04$), the rate is consistent with the full cluster rate.

7. DISCUSSION AND CONCLUSIONS

7.1. *Host-less Cluster SNe Ia*

As reported by Dawson09, we have discovered one potential host-less cluster SN Ia among the 8 ± 1 cluster SNe Ia. SN SCP06C1 is projected near two possible host galaxies: A $z_{850} = 21.6$ spiral galaxy $1''.1$ West of the SN, and a significantly fainter $z_{850} = 24.6$ galaxy $0''.45$ (~3.5 kpc at the cluster redshift) Northeast of the SN (See Dawson09, Fig. 2).

The galaxy-subtracted SN spectrum clearly shows a SN Ia at redshift $z = 0.98$ near maximum light, consistent with the light curve fit. The redshift of $z = 0.98 \pm 0.01$ is consistent with the cluster redshift of 0.974. The bright spiral galaxy is actually in the background of the cluster, at $z = 1.091$. Strong [OII] emission is visible in the spectrum, along with Ca H & K and Hδ absorption. Unfortunately, the small separation between the main galaxy and the smaller galaxy to the Northeast means that the spectrum of the smaller galaxy is dominated by light from the larger galaxy, making it impossible to assess a redshift. It is thus possible that the small galaxy is at the cluster redshift and is the actual host of the SN. Alternatively, the small galaxy might be at the same redshift as the larger galaxy and physically associated with it (either as a satellite galaxy or as part of the spiral structure of the galaxy).

We might hope to gain insight into the host from the SN parameters. We expect the intracluster medium to host an old stellar component. SNe occurring in this population would have parameters similar to those in passive elliptical galaxies, namely a low stretch value. If the stretch were $\gtrsim 1.2$, we might be able to conclude that the SN came from a young population (e.g., Brandt et al. 2010). However, the stretch of SN SCP06C1 is approximately 1.0 (Suzuki et al., in preparation), which is on the high side of the distribution in passive galaxies, but not unusual.

It is interesting to note that the SN is only $20''$ (160 kpc) projected radius from the center of the cluster, perhaps giving more weight to the hypothesis that it is associated with a diffuse intracluster stellar component.

Not being able to confirm or reject this SN as host-less, we have an upper limit of one host-less SN out of a total of 8 ± 1. Discovering one host-less SNe Ia out of seven total would imply an intrinsic host-less SN Ia fraction of $14\%^{+18\%}_{-7\%}$ (binomial 68% confidence intervals), and a 95% upper limit of $< 47\%$. These confidence intervals are similar to those of lower-redshift host-less SN Ia constraints (Gal-Yam et al. 2003; Sharon et al. 2010) (although Gal-Yam et al. were able to confirm the host-less nature of their SNe using deeper follow-up imaging). The upper limit is consistent with direct measurements of intracluster light at low redshift, but does not strongly constrain evolution. A sample twice the size or larger, with deeper follow-up to confirm host-less SNe Ia would begin to place interesting constraints on hypotheses for the formation of the intracluster stellar component from $z > 1$ to today.

7.2. *Comparison to Other Cluster Rate Measurements*

Cluster SN Ia rates have been reported at lower redshifts by several groups. In nearby ($z \lesssim 0.2$) clusters, measurements include those of Sharon et al. (2007) at $z \sim 0.14$, Mannucci et al. (2008) at $z \sim 0.02$, and Dilday et al. (2010) at $z \sim 0.09$ and $z \sim 0.22$. At intermediate redshifts, Sharon et al. (2010) recently reported the rate in $0.5 <$

$z < 0.9$ clusters (median $z \sim 0.6$). At higher redshifts, Gal-Yam et al. (2002) placed the first constraints on the $z \gtrsim 0.8$ cluster rate using a sample of three clusters at $z = 0.83$, 0.89 and $z = 1.27$. However, their SN sample included only one firm SN Ia at $z = 0.83$. The resulting rate has correspondingly large uncertainties and essentially places only an upper limit on the $z > 0.9$ cluster rate. Our result is thus a large step forward in the measurement of the SN rate in the highest-redshift clusters.

In Figure 14 we compare our full cluster rate to the lower-redshift rate measurements that have been normalized by stellar mass, permitting a comparison across redshifts. Here we have made an adjustment to the value reported by Sharon et al. (2010). Sharon et al. used the mass-to-light ratio of Bell03 for the SDSS g and r bands, but did not apply a correction for evolution between $z \sim 0.6$ and $z = 0$. Using the method described in §5.7 we find that a -0.14 dex offset should be applied to the mass to account for evolution from $z = 0.6$ to $z = 0$ (Fig. 11, *right panel*). We therefore adjust the reported rate of Sharon et al. upward by 0.14 dex (38%). The rate compilation of Maoz10 reflects this adjustment. Whereas the adjusted Sharon et al. rate shows an indication that the cluster rate is increasing with redshift, for the first time we find an increasing rate with high significance ($> 2\sigma$).

We point out that the popular "$A + B$" model (Scannapieco & Bildsten 2005) is insufficient for describing the change in cluster rate with redshift. In this model the SN rate is the sum of a term proportional to the total stellar mass and a term proportional to the recent star formation rate: $\mathcal{R}_{\rm SN\ Ia} = AM_* + B\dot{M}_*$. This simple model is convenient for predicting the SN rate in environments with varying amounts of recent star formation as it accounts for the increased SN Ia rate at short delay times. (In fact, we use this model in Meyers10 to derive limits on the expected ratio of SNe Ia to SNe CC in early-type galaxies.) However, beyond the fact that it matches predictions of an increased rate at short delay times, it is not theoretically motivated. In particular, it is not detailed enough to describe the cluster rate observations: In clusters, the A component is dominant at all redshifts observed. As M_* is not changing significantly with redshift, the rate would be expected to remain constant under this model. To describe these observations, we require a DTD model wherein the rate decreases at large delay times (as it does in most theoretically-motivated models).

7.3. *The Cluster SN Ia Delay Time Distribution*

To illustrate the cluster rate constraints on the DTD, We parameterize the late-time delay time distribution with a power law in time, $\Psi(t) \propto t^s$. A power law is not only a convenient parameterization in the face of limited data, but is a theoretically-motivated function for the DD scenario, where the late-time ($t \gtrsim 1$ Gyr) DTD shape is set by the distribution of WD separation after the second CE phase (Greggio 2005).

The cluster rates constrain $\Psi(t)$ from delay times of a few Gyr to ~ 10 Gyr. Here, we assume that the cluster ages correspond to the elapsed time since a formation redshift of $z_f = 3$ (Fig. 14). This is consistent with measurements of cluster elliptical galaxies showing that star formation was mostly completed by this redshift (e.g., Gobat et al. 2008). Our rate measurements in red and early-type galaxies provide a good consistency check that recent star formation does not significantly contribute to the SN Ia rate: if it did, we would ob-
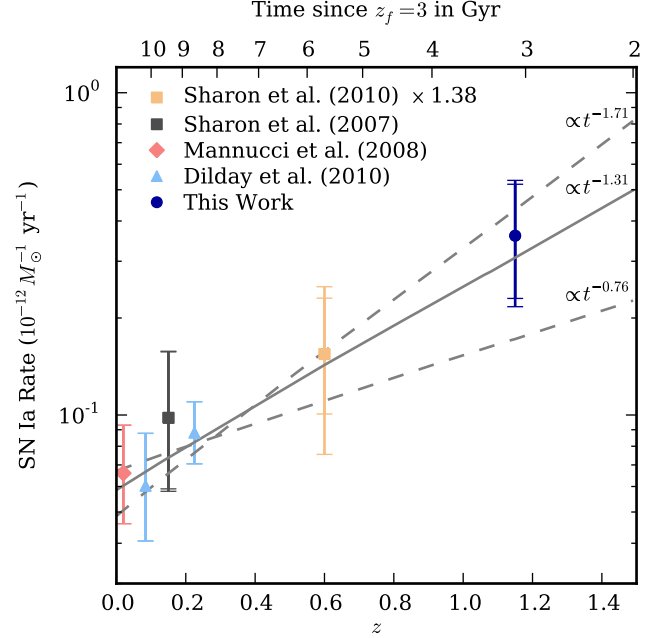

Figure 14. Cluster rate measurements (all galaxy types) from this work and the literature. The rate of Sharon et al. (2010) shown has been adjusted upward by 38% from the reported rate (see text). The top axis shows the time elapsed since an assumed cluster formation redshift of $z_f = 3$. The *solid grey line* represents the best-fit power-law DTD ($\Psi(t) \propto t^s$), while the *dotted grey lines* show the range of 1σ error on s.

serve a higher rate in the full cluster than in these subsamples. Mannucci et al. (2008) find similar limits on the contribution to the cluster rate from late-type galaxies at low redshift.

With the inferred stellar ages, the cluster rate measurements can be interpreted as the DTD, after a correction: the cluster rate measurements are normalized by *current* stellar mass whereas the DTD is normalized by *initial* stellar mass. The DTD, $\Psi(t)$ is therefore related to the cluster rate by $\Psi(t) = m(t)\mathcal{R}_{\rm SN\ Ia}(t)$ where $m(t)$ is the fraction of stellar mass remaining at time t after the star formation burst. Stellar population synthesis models (e.g., BC03 or PÉGASE2) show that over the age range of interest (~ 3 to 11 Gyr) the stellar mass declines by about 10%. We follow Maoz10 in using the stellar mass decline tabulated by BC03, but corrected by $m(t) = 1 - 0.7m_{\rm loss}(t)$ to effectively convert from the Salpeter IMF used in BC03 to a "diet" Salpeter IMF. We find a best-fit value of

$$s = -1.31^{+0.55}_{-0.40}, \tag{13}$$

and in Figure 14, we plot $\mathcal{R}_{\rm SN\ Ia}(t) = \Psi(t)/m(t)$ for this value. The χ^2 of the best-fit model is particularly small: 0.76 for 4 degrees of freedom. (The probability of finding a smaller χ^2 value is $\sim 6\%$.) Varying our assumption of $z_f = 3$ does not have a significant impact on the results, given the measurement uncertainty. With $z_f = 4$, we find $s = -1.43$ and with $z_f = 2.5$, $s = -1.21$. (See Maoz10 for a detailed treatment of variations from the single-burst assumption.)

This result is consistent with measurements of the late-time DTD in the field (Totani et al. 2008). It is also consistent with the value of $s \sim -1$ typically predicted for the DD scenario (but note that this prediction can vary depending on the distribution of WD separation). Most predictions for the

SD scenario show a steeper late-time DTD ([Greggio 2005](); [Ruiter et al. 2009](); [Mennekens et al. 2010]()) with an effective value for s ranging from $s \sim -1.3$ ([Greggio 2005]()) to $s < -3$ ([Mennekens et al. 2010]()). However, some groups have found that the SD scenario could be consistent with $s \sim -1$ given the right combination of main sequence and red giant secondaries ([Hachisu et al. 2008]()).

7.4. *Conclusions*

In this paper, we have made a measurement of the high-redshift cluster SN Ia rate. Thanks to an unusually complete dataset (particularly for a rate study) the measurement is quite robust, with statistical and systematic uncertainties on par with or better than measurement uncertainties at low redshift. We highlight several important and/or unique aspects of the measurement:

- The SN classification approach takes advantage of all relevant information. Thanks to the "rolling search" strategy of the survey and the nearly complete spectroscopic follow-up, most candidates have a full light curve and a host galaxy redshift, greatly reducing classification uncertainty.

- The position-dependent control time allows one to calculate a supernova rate given an arbitrary observing pattern and luminosity distribution.

- The control time calculation includes a full distribution of SN properties and the systematic uncertainty associated with the assumed distribution is carefully quantified. Thanks to the depth of the observations, the detection efficiency approaches 100% during the period of the survey for most of the clusters, meaning that the systematic uncertainty is low.

- Statistical uncertainties associated with the cluster luminosities, including both statistical variations and cosmic variance, are included in the total uncertainty. Also, light in the outskirts of each galaxy (outside the SEXTRACTOR MAG_AUTO aperture) is accounted for. This is a significant component of the total cluster luminosity.

- Cluster SN Ia rate measurements are normalized consistently across redshifts using a redshift-dependent mass-to-light versus color relation.

For the first time our result shows at the $> 2\sigma$ level that the cluster SN Ia rate is increasing with redshift. Simply by comparing the low- and high-redshift cluster rate measurements, the shape of the late-time SN Ia delay time distribution can be constrained. The power of the measurement for this purpose comes both from the high redshift and relatively low statistical and systematic uncertainties in the measurement. While we cannot conclusively rule out either the single degenerate or double degenerate class of progenitors via the delay time distribution, the binary evolution that could lead to each model are constrained. The DD scenario is consistent with the measurement under a wide range of plausible binary evolution parameters, while there is a stronger constraint on binary scenarios that could lead to an SD scenario. Finally, this measurement is unique in constraining the delay time distribution at delay times of a few Gyr. In future studies, it can be used in combination with other cluster rates and other delay time distribution measurements (e.g., Maoz10) to place even tighter constraints on models for binary evolution and SN Ia progenitor scenarios.

REFERENCES

Amanullah, R., et al. 2010, ApJ, 716, 712
Andreon, S. 2006a, in The Fabulous Destiny of Galaxies: Bridging Past and Present, ed. V. Le Brun, A. Mazure, S. Arnouts, & D. Burgarella, 463
Andreon, S. 2006b, MNRAS, 369, 969
—. 2006c, A&A, 448, 447
—. 2008, MNRAS, 386, 1045
Andreon, S., de Propris, R., Puddu, E., Giordano, L., & Quintana, H. 2008a, MNRAS, 383, 102
Andreon, S., Puddu, E., de Propris, R., & Cuillandre, J. 2008b, MNRAS, 385, 979
Andreon, S., Valtchanov, I., Jones, L. R., Altieri, B., Bremer, M., Willis, J., Pierre, M., & Quintana, H. 2005, MNRAS, 359, 1250
Astier, P., et al. 2006, A&A, 447, 31
Aubourg, É., Tojeiro, R., Jimenez, R., Heavens, A., Strauss, M. A., & Spergel, D. N. 2008, A&A, 492, 631
Barbary, K., et al. 2009, ApJ, 690, 1358
Belczynski, K., Bulik, T., & Ruiter, A. J. 2005, ApJ, 629, 915
Bell, E. F., McIntosh, D. H., Katz, N., & Weinberg, M. D. 2003, ApJS, 149, 289 (Bell03)
Bertin, E. & Arnouts, S. 1996, A&AS, 117, 393
Bohringer, H., Mullis, C., Rosati, P., Lamer, G., Fassbender, R., Schwope, A., & Schuecker, P. 2005, The Messenger, 120, 33
Brandt, T. D., Tojeiro, R., Aubourg, É., Heavens, A., Jimenez, R., & Strauss, M. A. 2010, AJ, 140, 804
Bremer, M. N., et al. 2006, MNRAS, 371, 1427
Brodwin, M., et al. 2006, ApJ, 651, 791
Bruzual, G. & Charlot, S. 2003, MNRAS, 344, 1000 (BC03)
Butcher, H. & Oemler, Jr., A. 1978, ApJ, 219, 18
—. 1984, ApJ, 285, 426
Cain, B., et al. 2008, ApJ, 679, 293
Calura, F., Matteucci, F., & Tozzi, P. 2007, MNRAS, 378, L11
Cappellaro, E., Evans, R., & Turatto, M. 1999, A&A, 351, 459
Cardelli, J. A., Clayton, G. C., & Mathis, J. S. 1989, ApJ, 345, 245
Chatzopoulos, E., Wheeler, J. C., & Vinko, J. 2009, ApJ, 704, 1251
Crawford, S. M., Bershady, M. A., & Hoessel, J. G. 2009, ApJ, 690, 1158
Dawson, K. S., et al. 2009, AJ, 138, 1271 (Dawson09)
Dilday, B., et al. 2010, ApJ, 713, 1026
Eisenhardt, P. R. M., et al. 2008, ApJ, 684, 905
Elston, R. J., et al. 2006, ApJ, 639, 816
Feldmeier, J. J., Ciardullo, R., & Jacoby, G. H. 1998, ApJ, 503, 109
Feldmeier, J. J., Ciardullo, R., Jacoby, G. H., & Durrell, P. R. 2004, ApJ, 615, 196
Ferguson, H. C., Tanvir, N. R., & von Hippel, T. 1998, Nature, 391, 461
Fioc, M. & Rocca-Volmerange, B. 1997, A&A, 326, 950
Fruchter, A. S. & Hook, R. N. 2002, PASP, 114, 144

Gal-Yam, A., Maoz, D., Guhathakurta, P., & Filippenko, A. V. 2003, AJ, 125, 1087

Gal-Yam, A., Maoz, D., & Sharon, K. 2002, MNRAS, 332, 37

Gänsicke, B. T., Levan, A. J., Marsh, T. R., & Wheatley, P. J. 2009, ApJ, 697, L129

Giavalisco, M., et al. 2004, ApJ, 600, L93

Gilbank, D. G., Yee, H. K. C., Ellingson, E., Hicks, A. K., Gladders, M. D., Barrientos, L. F., & Keeney, B. 2008, ApJ, 677, L89

Gobat, R., Rosati, P., Strazzullo, V., Rettura, A., Demarco, R., & Nonino, M. 2008, A&A, 488, 853

Gonzalez, A. H., Zabludoff, A. I., & Zaritsky, D. 2005, ApJ, 618, 195

Gonzalez, A. H., Zabludoff, A. I., Zaritsky, D., & Dalcanton, J. J. 2000, ApJ, 536, 561

Goto, T., et al. 2002, PASJ, 54, 515

Goto, T., et al. 2005, ApJ, 621, 188

Greggio, L. 2005, A&A, 441, 1055

Greggio, L. & Renzini, A. 1983, A&A, 118, 217

Guy, J., Astier, P., Nobili, S., Regnault, N., & Pain, R. 2005, A&A, 443, 781

Hachisu, I., Kato, M., & Nomoto, K. 2008, ApJ, 683, L127

Hakobyan, A. A., Petrosian, A. R., McLean, B., Kunth, D., Allen, R. J., Turatto, M., & Barbon, R. 2008, A&A, 488, 523

Hamuy, M., Trager, S. C., Pinto, P. A., Phillips, M. M., Schommer, R. A., Ivanov, V., & Suntzeff, N. B. 2000, AJ, 120, 1479

Hicken, M., Wood-Vasey, W. M., Blondin, S., Challis, P., Jha, S., Kelly, P. L., Rest, A., & Kirshner, R. P. 2009, ApJ, 700, 1097

Hicks, A. K., et al. 2008, ApJ, 680, 1022

Hilton, M., et al. 2007, ApJ, 670, 1000

Hsiao, E. Y., Conley, A., Howell, D. A., Sullivan, M., Pritchet, C. J., Carlberg, R. G., Nugent, P. E., & Phillips, M. M. 2007, ApJ, 663, 1187

Iben, Jr., I. & Tutukov, A. V. 1984, ApJS, 54, 335

Kessler, R., et al. 2009, ApJS, 185, 32

Kobayashi, C. & Nomoto, K. 2009, ApJ, 707, 1466

Koekemoer, A. M., Fruchter, A. S., Hook, R. N., & Hack, W. 2002, in The 2002 HST Calibration Workshop : Hubble after the Installation of the ACS and the NICMOS Cooling System, ed. S. Arribas, A. Koekemoer, & B. Whitmore, 337

Kowalski, M., et al. 2008, ApJ, 686, 749

Krick, J. E., Bernstein, R. A., & Pimbblet, K. A. 2006, AJ, 131, 168

Kuznetsova, N., et al. 2008, ApJ, 673, 981

Kuznetsova, N. V. & Connolly, B. M. 2007, ApJ, 659, 530

Li, W., et al. 2010, submitted (arXiv:1006.4612)

Lin, Y.-T. & Mohr, J. J. 2004, ApJ, 617, 879

Livio, M. 2001, in Supernovae and Gamma-Ray Bursts: the Greatest Explosions since the Big Bang, ed. M. Livio, N. Panagia, & K. Sahu, 334–355

Loewenstein, M. 2006, ApJ, 648, 230

Mannucci, F., Della Valle, M., & Panagia, N. 2006, MNRAS, 370, 773

Mannucci, F., Della Valle, M., Panagia, N., Cappellaro, E., Cresci, G., Maiolino, R., Petrosian, A., & Turatto, M. 2005, A&A, 433, 807

Mannucci, F., Maoz, D., Sharon, K., Botticella, M. T., Della Valle, M., Gal-Yam, A., & Panagia, N. 2008, MNRAS, 383, 1121

Maoz, D. & Gal-Yam, A. 2004, MNRAS, 347, 951

Maoz, D., Sharon, K., & Gal-Yam, A. 2010, ApJ, 722, 1879 (Maoz10)

Matteucci, F. & Greggio, L. 1986, A&A, 154, 279

Matteucci, F. & Recchi, S. 2001, ApJ, 558, 351

Melbourne, J., et al. 2007, AJ, 133, 2709

Mennekens, N., Vanbeveren, D., De Greve, J. P., & De Donder, E. 2010, A&A, 515, A89

Mihos, J. C., Harding, P., Feldmeier, J., & Morrison, H. 2005, ApJ, 631, L41

Morokuma, T., et al. 2010, PASJ, 62, 19

Mullis, C. R., Rosati, P., Lamer, G., Böhringer, H., Schwope, A., Schuecker, P., & Fassbender, R. 2005, ApJ, 623, L85

Nugent, P., Kim, A., & Perlmutter, S. 2002, PASP, 114, 803

Peng, C. Y., Ho, L. C., Impey, C. D., & Rix, H. 2002, AJ, 124, 266

Perlman, E. S., Horner, D. J., Jones, L. R., Scharf, C. A., Ebeling, H., Wegner, G., & Malkan, M. 2002, ApJS, 140, 265

Perlmutter, S., et al. 1999, ApJ, 517, 565

Perlmutter, S., et al. 1997, ApJ, 483, 565

Perlmutter, S., et al. 1995, ApJ, 440, L41

Postman, M., Lubin, L. M., & Oke, J. B. 2001, AJ, 122, 1125

Poznanski, D., Maoz, D., & Gal-Yam, A. 2007a, AJ, 134, 1285

Poznanski, D., et al. 2007b, MNRAS, 382, 1169

Pritchet, C. J., Howell, D. A., & Sullivan, M. 2008, ApJ, 683, L25

Quimby, R. M., et al. 2009, preprint (arXiv:0910.0059)

Richardson, D., Branch, D., Casebeer, D., Millard, J., Thomas, R. C., & Baron, E. 2002, AJ, 123, 745

Riess, A. G., et al. 1998, AJ, 116, 1009

Rix, H., et al. 2004, ApJS, 152, 163

Rosati, P., Stanford, S. A., Eisenhardt, P. R., Elston, R., Spinrad, H., Stern, D., & Dey, A. 1999, AJ, 118, 76

Rosati, P., et al. 2004, AJ, 127, 230

Rosati, P., et al. 2009, A&A, 508, 583

Ruiter, A. J., Belczynski, K., & Fryer, C. 2009, ApJ, 699, 2026

Ruiz-Lapuente, P., Burkert, A., & Canal, R. 1995, ApJ, 447, L69

Ruiz-Lapuente, P. & Canal, R. 1998, ApJ, 497, L57

Sánchez-Blázquez, P., Gorgas, J., Cardiel, N., & González, J. J. 2006, A&A, 457, 809

Santos, J. S., et al. 2009, A&A, 501, 49

Sarkar, D., Amblard, A., Cooray, A., & Holz, D. E. 2008, ApJ, 684, L13

Scannapieco, C., Tissera, P. B., White, S. D. M., & Springel, V. 2006, MNRAS, 371, 1125

Scannapieco, E. & Bildsten, L. 2005, ApJ, 629, L85

Schawinski, K. 2009, MNRAS, 397, 717

Schechter, P. 1976, ApJ, 203, 297

Sérsic, J. L. 1968, Atlas de galaxias australes, ed. Sérsic, J. L.

Sharon, K., et al. 2010, ApJ, 718, 876

Sharon, K., Gal-Yam, A., Maoz, D., Filippenko, A. V., & Guhathakurta, P. 2007, ApJ, 660, 1165

Sivanandam, S., Zabludoff, A. I., Zaritsky, D., Gonzalez, A. H., & Kelson, D. D. 2009, ApJ, 691, 1787

Soker, N., Frankowski, A., & Kashi, A. 2010, New A, 15, 189

Stanford, S. A., et al. 2005, ApJ, 634, L129

Stanford, S. A., Eisenhardt, P. R., & Dickinson, M. 1998, ApJ, 492, 461

Stanford, S. A., Holden, B., Rosati, P., Eisenhardt, P. R., Stern, D., Squires, G., & Spinrad, H. 2002, AJ, 123, 619

Stanford, S. A., et al. 2006, ApJ, 646, L13

Strazzullo, V., et al. 2006, A&A, 450, 909

Strolger, L.-G., et al. 2004, ApJ, 613, 200

Sullivan, M., et al. 2006, ApJ, 648, 868

Thielemann, F., Nomoto, K., & Hashimoto, M. 1996, ApJ, 460, 408

Thomas, D., Maraston, C., Bender, R., & Mendes de Oliveira, C. 2005, ApJ, 621, 673

Tornambe, A. 1989, MNRAS, 239, 771

Tornambe, A. & Matteucci, F. 1986, MNRAS, 223, 69

Totani, T., Morokuma, T., Oda, T., Doi, M., & Yasuda, N. 2008, PASJ, 60, 1327

Trenti, M. & Stiavelli, M. 2008, ApJ, 676, 767

Tsujimoto, T., Nomoto, K., Yoshii, Y., Hashimoto, M., Yanagida, S., & Thielemann, F. 1995, MNRAS, 277, 945

Tutukov, A. V. & Yungelson, L. R. 1994, MNRAS, 268, 871

van Dokkum, P. G., Franx, M., Kelson, D. D., & Illingworth, G. D. 2001, ApJ, 553, L39

Webbink, R. F. 1984, ApJ, 277, 355

Whelan, J. & Iben, I. J. 1973, ApJ, 186, 1007

Yungelson, L. R. 2005, in Astrophysics and Space Science Library, Vol. 332, White dwarfs: cosmological and galactic probes, ed. E. M. Sion, S. Vennes, & H. L. Shipman, 163–173

Yungelson, L. R. & Livio, M. 2000, ApJ, 528, 108

Zibetti, S., White, S. D. M., Schneider, D. P., & Brinkmann, J. 2005, MNRAS, 358, 949